

SMOS prototype algorithm for detecting autumn soil freezing



Kimmo Rautiainen^{a,*}, Tiina Parkkinen^a, Juha Lemmetyinen^a, Mike Schwank^{b,c}, Andreas Wiesmann^b, Jaakko Ikonen^a, Chris Derksen^d, Sergei Davydov^e, Anna Davydova^e, Julia Boike^f, Moritz Langer^f, Matthias Drusch^g, Jouni Pulliainen^a

^a Finnish Meteorological Institute, Arctic Research, P.O. Box 503, FI-00101 Helsinki, Finland

^b Gamma Remote Sensing AG, Worbstrasse 225, 3073 Gümligen, Switzerland

^c Swiss Federal Research Institute WSL, CH-8903 Birmensdorf, Switzerland

^d Environment Canada, Canada

^e North-East Science Station, Pacific Institute of Geography, Far-Eastern Branch, Russian Academy of Sciences, Cherskiy, Republic of Sakha (Yakutia) 678830, Russia

^f Alfred Wegener Institute, Helmholtz Center for Polar and Marine Research, Germany

^g European Space Agency, ESTEC, 2200 AG Noordwijk, The Netherlands

ARTICLE INFO

Article history:

Received 31 July 2015

Received in revised form 11 December 2015

Accepted 17 January 2016

Available online 9 February 2016

Keywords:

Microwave radiometry

Soil freeze/thaw

SMOS

ABSTRACT

A prototype algorithm for hemispheric scale detection of autumn soil freezing using space-borne L-band passive microwave observations is presented. The methodology is based on earlier empirical and theoretical studies of L-band emission properties of freezing and thawing soils. We expand a method originally developed for soil freeze–thaw (F/T) state detection from L-band tower based observations to satellite scale, applying observations from the European Space Agency's Soil Moisture and Ocean Salinity (SMOS) mission. The developed algorithm is based on first establishing spatially variable thresholds for L-band brightness temperatures representing frozen and thawed states of soil, and comparing these to current values of different indicators of soil freezing, calculated based on observed brightness temperature at different polarizations and incidence angles. An exponential relation between the freezing indicators and the depth of soil frost is developed based on a large amount of manual soil frost tube observations across Finland. An additional processing filter based on observed physical temperature and snow cover information is used to flag obvious F/T detection errors. The estimated soil F/T-states provided in this study are limited to the autumn freezing period, as melting snow in spring effectively prevents acquisition of information from the soil surface using microwaves for large areas in Northern latitudes. The F/T estimate is produced as daily information and provided in the equal-area scalable Earth (EASE) grid. Soil F/T-state is categorized into three discrete levels: 'frozen', 'partially frozen', and 'thawed', and accompanied with a quality data matrix estimating the data reliability for each freezing season separately. Comparisons to *in situ* data were conducted at 10 different locations in Finland, Northern America and Siberia. These comparison results indicate that the onset of autumn soil freezing can be estimated from SMOS observations to within 1 to 14 days, depending on the freezing indicator applied and the *in situ* data used in comparison. Although the initial results are encouraging, more comprehensive assessment of SMOS based soil F/T estimates still requires further comparison to other reference sites, particularly to sites with measurements available for all locally representative land cover types, as well as other satellite-based soil freezing products.

© 2016 The Authors. Published by Elsevier Inc. This is an open access article under the CC BY license (<http://creativecommons.org/licenses/by/4.0/>).

1. Introduction

The European Space Agency's SMOS (Soil Moisture and Ocean Salinity) satellite mission (Kerr et al., 2010) provides regular low-frequency (L-band, 1–2 GHz) passive microwave observations (brightness temperatures) from space. The original geophysical parameters sought by SMOS, soil moisture and ocean salinity, have recently been

complemented by initiatives to retrieve additional variables such as surface roughness (Fernandez-Moran et al., 2014), vegetation optical depth (Lawrence et al., 2014), thin sea ice (Kaleschke, Tian-Kunze, Maaß, Mäkynen, & Drusch, 2012), and the freeze/thaw (F/T) state of soils (Schwank et al., 2004; Rautiainen et al., 2012, 2014).

Information on the state of aggregation of soil is essential for diverse hydrological, biogeochemical, and climatological applications. Soil freezing has an effect on surface energy balance, surface and subsurface water flow, and exchange rates of carbon with the atmosphere (Skogland, Lomeland, & Goksoyr, 1988; Zhang, Barry, Knowles, Ling, & Armstrong, 2003; Zhang, Zhao, Jiang, & Zhao, 2010; Langer,

* Corresponding author at: Finnish Meteorological Institute, Arctic Research, P.O. Box 503, FI-00101 Helsinki, Finland.

E-mail address: Kimmo.rautiainen@fmi.fi (K. Rautiainen).

Westermann, Muster, Piel, & Boike, 2011). In addition, soil freezing controls important biogeochemical processes such as the photosynthetic activity of plants and the microbial activity within soils (Hollinger et al., 1999; Liebner et al., 2015).

Large areas in the Northern Hemisphere are characterized by perennially or seasonally frozen soils. Seasonal freezing occurs on approximately 51% of the land surface, while permafrost areas cover approximately 24% (Smith & Brown, 2009). Remote sensing from space is a viable option to provide timely information on soil F/T processes on a hemispheric scale. Detection of soil F/T-states by means of Earth Observation requires a remote sensing technique with sufficient penetration into the soil medium. While this precludes the use of optical wavelengths, both active- and passive microwave sensors can provide information on the surface F/T state (Zuerndorfer & England, 1992; Rignot & Way, 1994; Kim, Kimball, Zhang, & McDonald, 2012). The detection of the soil F/T-state is also a goal of the NASA (National Aeronautics and Space Administration) SMAP (Soil Moisture Active–Passive) mission, launched in January 2015. This satellite carries a radiometer (passive) and a SAR (active), both operating in the microwave L-band; SMAP applies the active sensor for soil F/T detection (Entekhabi et al., 2010). A surface soil state flag has also been developed for the ASCAT (Advanced Scatterometer) instrument (Naemi et al., 2012). Kim, Kimball, McDonald, and Glassy (2011) and Zhao et al. (2011) have developed F/T algorithms for higher frequency passive instruments such as the Special Sensor Microwave Imager (SSM/I) and the Advanced Microwave Scanning Radiometer Enhanced (AMSR-E), respectively.

Compared to data products based on microwave sensors operating at higher frequencies (e.g. Kim et al., 2011), L-band observations exhibit deeper soil penetration depths, reduced influence from overlying vegetation, and hence increased sensitivity to the freezing process (Rautiainen et al., 2014). Consequently, experimental work has provided clear indications of the viability of L-band passive microwave observations for the purpose of soil F/T monitoring (Schwank et al., 2004; Rautiainen et al., 2012, 2014). The physical mechanism for the detection of soil freezing from passive microwave observations is as follows: The presence of free liquid water in soils causes high effective permittivities of unfrozen wet soils (e.g. Wang & Schmugge, 1980; Mironov, Muzalevskiy, & Savin, 2013; Mätzler, Ellison, Thomas, Sihvola, & Schwank, 2006). Accordingly, L-band emissivities (and thus L-band brightness temperatures) exhibit a pronounced negative correlation with liquid soil water-content, which is utilized in SMOS based soil moisture retrieval (Wigneron et al., 2007). On the other hand, freezing of free liquid water in soils decreases effective soil permittivities, and thus increases emissivities and thus brightness temperatures significantly. The strong positive correlation between L-band brightness temperature and the freezing of free liquid water is fundamental for the F/T retrieval algorithm outlined in this study.

Using experimental data, Rautiainen et al. (2014) explored several possibilities for a soil F/T-state algorithm based on detecting changes in the dual-polarized ($p = H, V$) L-band brightness temperatures T_B^p . This investigation focused on two features apparent from ground-based measurements T_B^p , i.e. an increase and subsequent saturation of brightness temperatures T_B^p with soil freezing, as well as a decrease in differences $T_B^V - T_B^H$ between brightness temperatures at vertical ($p = V$) and horizontal ($p = H$) polarization. These features are explained by the previously mentioned decrease of the effective soil permittivity with freezing, and can thus be exploited to analyze the F/T-state of the soil by applying a relatively simple change detection algorithm. Rautiainen et al. (2014) proposed establishing reference levels from summer and winter observations in order to calculate a so-called frost factor for each pixel observed. With comparisons to *in situ* soil frost depth observations, a threshold was established to identify the freezing of soil surface-layers up to 10 cm depth. Different combinations of polarization ($p = H, V$), observation angle, and degrees of temporal averaging were investigated to reach the best possible performance of the F/T change detection approach. The method, initially developed

for sandy mineral soils, was also applied to T_B^p measured over a wetland site at the FMI-ARC (Finnish Meteorological Institute Arctic Research Centre) in Sodankylä, Finland (Lemmetyinen et al. (under review)). The results indicated that adaptation of the F/T algorithm will likely require tuning the frost factor thresholds to account for land cover and soil type heterogeneities within given pixels observed by the SMOS satellite as illustrated by Roy et al. (2015) using SMOS and Aquarius data over Canada. Recent theoretical studies (Schwank et al., 2014, 2015), corroborated by experimental investigations (Lemmetyinen et al., under review), have shown that passive L-band observations T_B^p are also sensitive to dry snow cover, in particular at horizontal polarization. Before this recognition L-band brightness temperatures T_B^p were assumed to be insensitive with respect to dry snow due to its acknowledged low extinction at L-band. However, the theoretical investigation of Schwank et al. (2015) revealed that refraction and impedance matching caused by dry snow explains the observed sensitivity of L-band T_B^p with respect to the density to the bottom layer of snow (~10 cm). As outlined in detail in Schwank et al. (2014), the impact of refraction and impedance matching caused by dry snow on the L-band emission of ground-surfaces covered with dry snow is to influence L-band brightness temperatures in the same direction as is caused by soil freezing hence inducing uncertainty for the soil F/T-state detection algorithms.

In this study, we expand the algorithm introduced by Rautiainen et al., 2014 to the satellite scale, presenting a prototype algorithm for detecting the autumn soil freeze state from SMOS brightness temperature observations. The algorithm is based on establishing spatially variable (pixel-wise) thresholds for brightness temperatures representing frozen and thawed surface states. An additional processing filter based on observed physical temperature and snow cover information is used to exclude obvious detection errors and to establish a reliability flag for the SMOS soil F/T-state estimate.

2. Data

This study uses space borne passive L-band observations (brightness temperatures T_B^p) from the SMOS mission, automated and manual *in situ* measurements of soil temperature and freezing depth from reference test sites, as well as global ancillary datasets for climatological classification of ground temperature. The investigated study period is from February 2010 until December 2014, covering four autumn freezing seasons across the northern hemisphere.

2.1. Brightness temperature observations

The sole payload instrument of SMOS is MIRAS (Microwave Imaging Radiometer with Aperture Synthesis) (Martin-Neira & Goutule, 1997) which measures radiation emitted from the Earth at the protected portion (1400 MHz–1427 MHz) of the L-band (1 GHz–2 GHz). SMOS is in a sun synchronous orbit crossing the equatorial node at 6 am local time during the ascending pass and 6 pm during the descending pass. The measurement principle is based on two-dimensional aperture synthesis, where the image of the target is reconstructed from simultaneous measurements (so called ‘visibilities’) of multiple receivers (Khazaal & Anterrieu, 2009). SMOS provides multi-angular, fully polarized brightness temperatures at a spatial resolution of 43 km on average over the globe with a revisit time of less than three days (Kerr et al., 2001). This is of great advantage to many remote sensing applications relying on full global coverage and high temporal resolution. However, due to the interferometric measurement principle MIRAS has a slightly reduced sensitivity and increased noise compared to conventional real aperture radiometers; the radiometric sensitivity (target noise temperature 220 K, integration time 1.2 s) is 3.5 K (boresight) and 5.8 K (edge of swath) (Mecklenburg et al., 2012). Despite the choice of the protected frequency band (1400 MHz–1427 MHz) reserved for radio astronomy, anthropogenic Radio Frequency Interference (RFI) can be regionally prevalent (Oliva et al. (2012)). The systematic error

for SMOS brightness temperatures over RFI free areas has been estimated to be in the order of 2.5 K (Mecklenburg et al., 2012).

In this study, SMOS level 3 brightness temperatures T_B processed by CATDS (Centre Aval de Traitement des Données SMOS) are applied. The data are daily gridded, transformed from the satellite reference frame to the ground polarization reference frame $p = H$ (horizontal), V (vertical) and provided in the global Equal-Area Scalable Earth Grid (EASE-Grid). Multi-angular SMOS level 3 $T_B(\theta)$ are averaged into fixed observation angles θ binned at 5 degree intervals.

2.2. Reference in situ data

2.2.1. Frost tube network over Finland

The Finnish Environment Institute's (SYKE) soil frost monitoring network is used as the main ground reference in optimizing the SMOS F/T algorithm. The network consists of manual frost tube measurements at 38 locations around Finland. The distribution of these stations is depicted in Fig. 1. Frost tubes are installed at sites representing three classes of land cover (forest, open areas and wetlands), if all of these are present at the location. Typically, measurements are conducted three times a month, with supplementary measurements taken during freezing and thawing periods. The frost tubes consist of Chlorinated Polyvinyl Chloride (CPVC) tubes containing a mixture of water and a food colorant. The colorant changes with freezing, allowing visual estimation of frost depth FD . The frost tubes in the SYKE network measure freezing down to a depth of $FD = 2$ m. Iwata et al. (2012) have studied the accuracy of frost tube measurements finding a 2.8 cm root mean square error (rmse) when comparing frost tube observations against frost depths estimated from measured soil temperature profiles. SYKE estimates the overall accuracy of their tube readings to be ± 5 cm (Mäkinen & Orvoma, 2012).

2.2.2. Soil moisture and soil temperature in situ sites

Various geographically distributed sources of *in situ* data have been selected to compare the SMOS based soil F/T estimate against *in situ* data. These ground reference stations include the FMI sites in Sodankylä and Rovaniemi, Finland, the SNOTEL (Snow Telemetry) network sites in Alaska (Leavesley et al., 2010), three sites in the Siberian permafrost zone, The North-East Science Station in Cherskii at river Kolyma and the Russian Research Station Samoylov, the Tiksi International Hydrometeorological Observatory, and a soil moisture network maintained by Environment Canada near Kenaston, Saskatchewan. Next a short description of each site is provided, and summarized in Table 1.



Fig. 1. SYKE frost tube locations in Finland.

The FMI Sodankylä site is located in Finnish Lapland representing a typical flat northern boreal forest/taiga environment. This study uses soil moisture and soil temperature (Decagon TE5 sensors) data from an automatic observation network covering all typical soil types and land cover classes found in the area. FMI also hosts a WMO (World Meteorological Organization) station in Rovaniemi, in Northern Finland, which includes soil temperature (PT100 thermistor) profile measurements from 5 cm to 2 m depth. The measurement sensors located at the Rovaniemi site have been installed on an open field while the surrounding area is mostly covered with boreal forests. It is an example of a test site that poorly represents the surrounding area.

SNOTEL sites are operated and maintained by the Natural Resources Conservation Service (Zreda et al., 2011). The data used in our study have been gathered through the International Soil Moisture Network (ISMN) (Dorigo et al., 2011, 2013). The data includes observations from five enhanced stations in Alaska, equipped with Stevens Hydraprobes soil moisture and temperature measurement sensors at SNOTEL standard depths of 5 cm, 10 cm, 20 cm and 50 cm (originally stated as 2, 4, 8 and 20 in.). Each site, Granite Creek, Monahan Flat, Eagle Summit, Upper Nome Creek, and Gobblers Knob, has at least four years of *in situ* data available through the ISMN. These sites have a minimal areal fraction of open water in the respective SMOS EASE grid cell.

The North-East Science Station is hosted by the Russian Academy of Science in Cherskii. The study area of soil temperature measurements is located in the Kolyma Lowland (the lower reaches of the Kolyma River) which is part of the Arctic Siberian Coastal Plains. The Kolyma region is characterized by continuous permafrost. The Cherskii Meteorological Station, which is located near the study area, indicated an average annual temperature of -11.6 °C and an average annual precipitation sum of 285 mm. The average number of snow cover days per year was 229. Snow typically sets in early October, melting at the end of May. The mean snow height at the site was 34 cm. The area is covered by a sparse larch (*Larix cajanderi*) forest with abundant small shrubs. The soil surface is typically covered by moss and lichen. Thermokarst wetlands and lakes occupy a significant part of the area. The basic soil types in the region are peaty gleyzem and gleyic cryozem soils. The soil composition is loess-like loam with rare detritus (Fyodorov-Davydov & Davydov, 2006).

Samoylov Island is located in Northern Yakutia, Siberia, in the Lena River Delta (Boike et al., 2013). Of all the sites used in this study, the surrounding area of the Samoylov Island site has the largest wetland fraction within the corresponding EASE grid-cell. According to GlobCover 2009 data it is approximately 20%. The tundra landscape on Samoylov Island is mainly characterized by ice-wedged polygons forming a highly fragmented land cover pattern consisting of wet depressed polygon centers surrounded by relatively dry polygon ridges (Boike et al., 2013). In addition, thermokarst lakes and ponds frequently occur (Muster, Langer, Heim, Westermann, & Boike, 2012). The soil moisture and temperature site includes sensors in elevated and relatively dry polygon ridges, and in a "wet" depression at the centre of the tundra polygon and on a slope in between the two (Boike et al., 2013).

The Tiksi International Hydrometeorological Observatory has been developed through a partnership between the National Science Foundation (NSF), the National Oceanic and Atmospheric Administration (NOAA), the Russian Federal Service for Hydrometeorology and Environmental Monitoring (Roshydromet), and FMI. Soil moisture (using Delta-T Thetaprobe ML2x) and temperature (PT100 sensors) data are available from a single location since July 2010. These sensors have been installed by FMI.

Environment Canada maintains a soil moisture network situated across a $10 \text{ km} \times 10 \text{ km}$ area of open cropland near Kenaston, Saskatchewan. There are 23 automatic stations each equipped with three Stevens Hydraprobes (calibrated for local soil conditions) at depths of 5 cm, 20 cm, and 50 cm measuring soil moisture and temperature.

Table 1

Reference sites providing the *in situ* measurements (VWC_G = volumetric soil water content, T_G = ground temperature). Site locations (latitude/longitude), its land classes, and the land class percentages (forest, open, wetland, water (GlobCover)) of the EASE grid pixel including the sites are provided.

Network/site		<i>In situ</i>	Lat. [°]	Lon. [°]	Land class	EASE land class percentage [%]			
Name	Owner					Forest	Open	Wetland	Water
Sodankylä	FMI	T_G/VWC_G	67.37	26.82	Boreal forest, Open, and wetland	83	11	5	1
Rovaniemi	FMI	T_G	66.58	26.01	Open field	86	10	3	1
Granite Crk	SNOTEL	T_G/VWC_G	63.95	−145.4	Boreal forest	64	35	0	< 1
Monahan Flat*	SNOTEL	T_G/VWC_G	63.3	−147.65	Boreal forest	22	53	0	0
Eagle Summit	SNOTEL	T_G/VWC_G	65.48	−145.42	Tundra	48	52	0	0
Upper Nome Creek	SNOTEL	T_G/VWC_G	65.37	−146.6	Sparse forest	40	60	0	0
Gobblers Knob	SNOTEL	T_G/VWC_G	66.75	−150.67	Tundra	45	55	0	0
Cherskii	Russian Academy of Science	T_G	68.73	161.4	Boreal forest	72	13	< 1	15
Samoylov**	Russian Research station	T_G/VWC_G	72.4	126.5	Tundra	6	66	20	8
Tiksi**	FMI	T_G/VWC_G	71.60	128.89	Tundra	1	94	0	5
Kenaston	EC***	T_G/VWC_G	51.4	−106.6	Agriculture	10	90	< 1	0

* The missing land class portion in Monahan flat is classified as others and is mostly glaciers.

** Contrary to GlobCover data the areas surrounding Tiksi and Samoylov sites do not have any forests, shrubs with higher normalized difference vegetation index (NDVI) are “misclassified” as forest in these northern latitudes.

*** Environment Canada.

For comparisons against SMOS soil freeze estimates only data from sensors at depths of 5 cm, from each site, were included in our analysis in order to maintain consistency. Table 1 provides information on the reference sites and on the corresponding EASE grid pixel.

2.3. Ancillary data

The global ancillary datasets listed below are required by the F/T algorithm for filtering unrealistic estimates of the freeze state.

- ECMWF ERA Interim analysis surface layer air temperature (2 m) data (Dee et al., 2011): The dataset covers the entire SMOS period (2010–2014). The data, originally at spatial resolution of $0.75 \times 0.75^\circ$, are re-projected to correspond with SMOS data. The dataset is used in the algorithm to determine summer and winter seasons (pixel-wise). This information is further applied to define the references of the frozen and thaw soil state and when creating the processing mask for the algorithm.
- The ESA data user element GlobCover 2009 data (Arino et al., 2012): The dataset is mainly used for acquiring sub-grid land cover information for the SMOS pixels.
- Daily snow cover data from the National Oceanic and Atmospheric Administration/National Environmental Satellite, Data, and Information Service (NOAA/NESDIS) Interactive Multisensor Snow and Ice Mapping System (IMS): The IMS dataset, derived from daily manual analysis of various satellite and *in situ* datasets (Helfrich, McNamara, Ramsay, Baldwin, & Kasheta, 2007) is used in creating the processing mask for the F/T algorithm.

3. Method

3.1. Background

Our soil F/T-state retrieval algorithm is based on detecting the annual changes in soil permittivity along with soil freezing and thawing. The effective permittivity of moist unfrozen soil drops distinctly when liquid soil-water (with permittivity of ≈ 80 at L-band) freezes to ice (with permittivity of ≈ 3 at the L-band) (see e.g. Mätzler, Ellison, Thomas, Sihvola, & Schwank, 2006). As a result, L-band brightness temperatures T_B^p at horizontal ($p = H$) and vertical ($p = V$) polarization emitted from frozen soil is generally higher than T_B^p measured above a thawed moist soil. Obviously, other parameters, such as the physical temperature of the scene observed, vegetation phenology, and subgrid heterogeneity affect T_B^p and can result in ambiguities in the retrieval of the soil F/T-state.

The soil state detection algorithm presented here draws substantially on an earlier study (Rautiainen et al., 2014) based on tower-based L-band brightness temperatures T_B^p measured with the ELBARA-II radiometer (Schwank et al., 2010). The study by Rautiainen et al. (2014) showed that soil freezing influences T_B^p in two distinct ways: i) T_B^p increases at horizontal ($p = H$) and vertical ($p = V$) polarization and ii) polarization difference $|T_B^H - T_B^V|$ decreases. Several definitions of a so-called frost factor (FF), serving as a radiometrically derived proxy for the soil freeze state, were formulated, involving SMOS T_B^H and T_B^V measurements. An empirical approach was used to identify the most successful definition of the FF yielding the highest correlation between retrieved and *in situ* observed soil F/T states.

Recent theoretical and experimental studies (Schwank et al., 2014, 2015; Lemmetyinen et al., accepted for publication) have shown that dry snow cover on top of frozen or non-frozen soil has a significant impact on L-band emission T_B^p due to refraction and impedance matching caused by dry snow. These snow propagation processes increase T_B^H at all observation angles, producing a signature similar to that of soil freezing. The effect of dry snow on T_B^V is much smaller than the effect on T_B^H , and practically negligible at observation angles near 50 degrees relative to nadir (Schwank et al., 2015; Lemmetyinen et al., accepted for publication). As a result, the polarization difference $|T_B^H - T_B^V|$ is significantly smaller when dry snow cover is present on top of soil, when compared to soil without snow cover. Work to date (such as Rautiainen et al., 2014) has not taken into consideration that the L-band response to soil freezing, i.e. the absolute level of brightness temperature, and the polarization difference, are also consistent with the response to dry snow cover, independent of the soil state. This has a potential complicating influence on F/T retrievals.

Based on theoretical predictions, the most successful definition of FF would be based solely on $T_B^V(\theta)$ measured at observation angles in the range of $50^\circ \leq \theta \leq 55^\circ$. This is because $T_B^V(\theta \approx 50^\circ)$ is predicted to be almost independent of the presence of dry snow as refraction and impedance matching caused by snow are expected to be compensated for $p = V$ and $\theta \approx 50^\circ$. However, when using $T_B^V(\theta \approx 50^\circ)$ exclusively to define the proxy FF for the soil freeze state, the detection of F/T is strongly affected by annual variation in the physical temperature of the observed scene. This generates challenges especially for areas with a continental climate where the annual dynamics of near-surface soil temperatures can be very large. The challenges are further increased if typical summer conditions for a given location are dry, since the difference in permittivity between dry and frozen soil is naturally small. For the aforementioned reasons, performance of soil F/T detection based exclusively on $T_B^V(\theta \approx 50^\circ)$ was degraded for large regions of the Northern Hemisphere. Accordingly, our soil F/T retrieval approach uses FF involving measurements of T_B^V augmented by retrievals using the

normalized polarization ratio (NPR) as is elaborated in the following Section.

3.2. Principle of the soil F/T retrieval

The soil F/T-state retrieval algorithm is based on pixel-wise frost factors FF derived from SMOS measurements T_B^p ($p = H, V$). For each pixel, FF is compared against pixel-wise thaw and freeze references. Accordingly, our F/T retrieval can be classified as a so-called “change detection approach”. Ultimately, a three-stage soil state category is applied by defining adequate thresholds of the soil freeze state proxy allowing a distinction between ‘frozen’, ‘partially frozen’, and ‘thawed’ soil states to be made. A schematic describing the generation of the soil state estimates is shown in Fig. 2, and the relevant steps are outlined subsequently:

In the first stage, SMOS CATDS daily gridded brightness temperatures T_B^p are converted to the Northern Hemisphere EASE-Grid. Data with poor quality are filtered out according to the following criteria:

1. Unrealistic brightness temperature values $T_B^p > 300\text{K}$ or $T_B^p < 70\text{K}$ ($p = H, V$),
2. Negative polarization difference $T_B^V < T_B^H$, and
3. Sudden unrealistic temporal changes in T_B^p values: $dT_B^p > 3 \cdot \text{STD}(dT_B^p)$, where dt is difference between successive measurements.

Ascending and descending SMOS orbits (orb) are processed separately due to different RFI conditions; e.g. the descending orbits over Asia and Siberia are more notably contaminated by RFI.

In the second stage, two different FF formulations are used to relate measurements of T_B^p to the F/T-state of the soil:

$$FF_{V,orb} \equiv 300 \text{ K} - T_{B,orb}^V, \quad (1)$$

$$FF_{\text{NPR},orb} \equiv \frac{T_{B,orb}^V - T_{B,orb}^H}{T_{B,orb}^V + T_{B,orb}^H}. \quad (2)$$

$FF_{V,orb}$ is thus solely based on V-polarization data, while $FF_{\text{NPR},orb}$ is based on the normalized polarization ratio NPR ($orb = \text{ascending, descending orbit}$). Time series of $FF_{V,orb}(t)$ and $FF_{\text{NPR},orb}(t)$ are produced separately for both $orb = \text{ascending and } orb = \text{descending}$. The resulting time series $FF_{X,orb}(t)$ ($X = V, \text{NPR}$) are further converted to relative (rel) frost factor values $FF_{\text{rel},X,orb}$ in units of percentage:

$$FF_{\text{rel},X,orb}(t) \equiv \frac{FF_{X,orb}(t) - FF_{\text{su},X,orb}}{FF_{\text{wi},X,orb} - FF_{\text{su},X,orb}} \cdot 100\%, \quad (3)$$

where $FF_{\text{wi},X,orb}$ and $FF_{\text{su},X,orb}$ are the empirically defined winter (wi) and summer (su) references for each pixel, respectively, defined for both FF formulations ($X = V, \text{NPR}$) and both orbits ($orb = \text{ascending, descending}$). The $FF_{\text{rel},X,orb}$ value of 100% equals the winter reference, while $FF_{\text{rel},X,orb} = 0\%$ corresponds with the summer reference. Temporal averaging can be applied to the relative frost factors $FF_{\text{rel},X,orb}$ in order to reduce the effect of short-term variations; in all analyses conducted in this study, an averaging window of 25 days was applied.

Ultimately, the time series of relative frost factors $FF_{\text{rel},X,orb}$ are compared to predefined thresholds, categorizing the observation into three discrete soil states (‘frozen’, ‘partially frozen’, ‘thawed’). In the final stage, a consolidated hemispheric-scale estimate is generated by applying a processing mask to mitigate clearly erroneous soil state estimates. The approach used to estimate the pixel-wise summer- and winter references ($FF_{\text{su},X,orb}$ and $FF_{\text{wi},X,orb}$, respectively), the categorization of the relative frost factors $FF_{\text{rel},X,orb}$ to distinguish between the three discrete soil states (‘frozen’, ‘partially frozen’, ‘thawed’), and the generation of the processing mask are described in more detail in the following Sections.

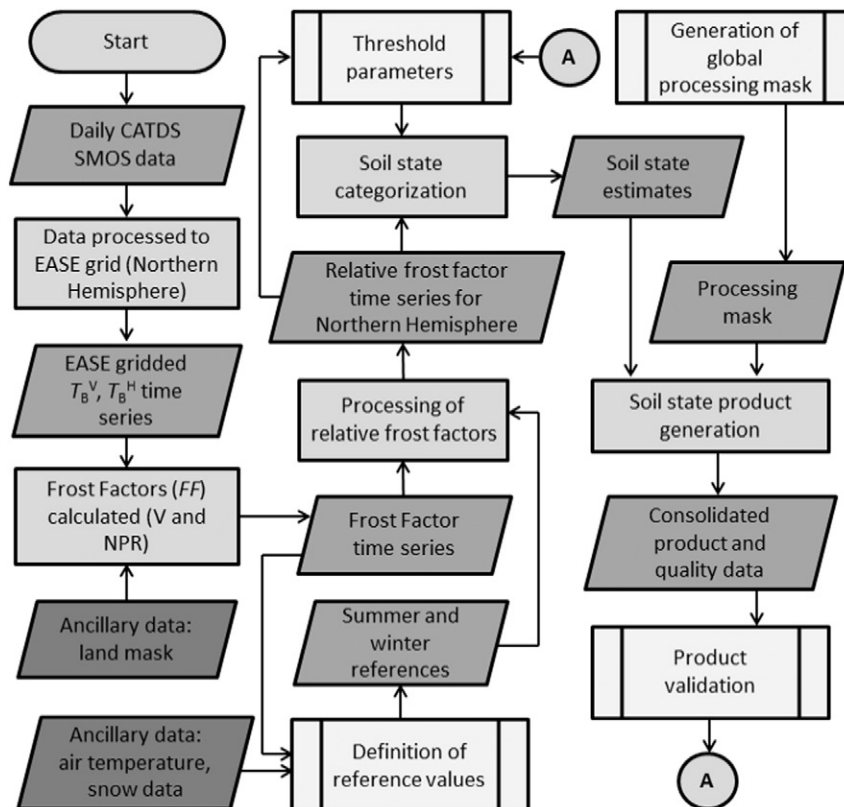


Fig. 2. Flow chart describing the soil state estimate generation from SMOS CATDS data and ancillary data to consolidate our soil F/T product.

3.3. Summer and winter references

Summer (su) and winter (wi) references $FF_{su,X,orb}$ and $FF_{wi,X,orb}$ ($X = V, NPR; orb = \text{ascending, descending}$) are defined for each pixel using all available historical SMOS data from June 2010 onwards. ECMWF T_{air} data, representing air temperature at 2 m above ground, are used to identify possible dates representing winter ('frozen') and summer ('thawed') periods. This identification is made individually for each grid cell, following the methodology shown in Fig. 3. If T_{air} is below the winter threshold (TR) $T_{TR,wi} = -3\text{ }^{\circ}\text{C}$, the corresponding date is considered to belong to the winter period. Similarly, for $T_{air} > T_{TR,su} = +3\text{ }^{\circ}\text{C}$ an observation is categorized as a summer measurement. In both cases, wet snow cover conditions are omitted.

In order to obtain winter references $FF_{wi,X,orb}$ ($X = V, NPR; orb = \text{ascending, descending}$) the average of the 30 lowest values of all available observations of $FF_{wi,X,orb}$ ($T_{air} < T_{TR,wi} = -3\text{ }^{\circ}\text{C}$) are selected, with the lowest 10 values omitted to protect against potential erroneous observations. The same logic is applied to obtain summer references $FF_{su,X,orb}$ by taking the average of 30 of the highest values of $FF_{su,X,orb}$ ($T_{air} > T_{TR,su} = +3\text{ }^{\circ}\text{C}$), while omitting the 10 highest values. The same pixel-wise reference values $FF_{wi,X,orb}$ and $FF_{su,X,orb}$ are applied for the whole time series of soil F/T retrievals in this study.

3.4. Categorization of soil state and parameter optimization

The relative frost factors $FF_{rel,X,orb}$ available for each pixel were assigned to the three soil state categories 'frozen', 'partially frozen', and 'thawed' based on pre-defined threshold values. The latter were initially acquired by comparing $FF_{rel,X,orb}$ derived for EASE gridded SMOS observations to collocated *in situ* frost depth FD available from the SYKE frost observation network, and the collocated *in situ* frost depths FD from Northern Finland. An empirical exponential model, including the fitting parameters $A_{X,orb}$ and $B_{X,orb}$, were used to relate relative frost factor $FF_{rel,X,orb}(FD)$ with frost depth FD :

$$FF_{rel,X,orb}(FD) = A_{X,orb} \cdot (1 - \exp(-B_{X,orb} \cdot FD)), \quad (4)$$

Table 2 provides the values of the fitting parameters $A_{X,orb}$ and $B_{X,orb}$ associated with the corresponding retrieval versions $X = V$ and $X = NPR$ (definitions (1) and (2)). Thereby, we considered ascending and descending SMOS brightness temperatures T_B^{θ} measured at the incidence angle range $50^{\circ} \leq \theta \leq 55^{\circ}$.

Table 2

Fitting parameters $A_{X,orb}$ and $B_{X,orb}$ calculated for the exponential model $FF_{rel,X,orb}(FD)$ associated with the two F/T detection versions $X = V$ and $X = NPR$. Here we used both, ascending and descending orbits ($orb = \text{ascending} + \text{descending}$).

	$A_{X,orb}$ (%)	$B_{X,orb}$ (cm^{-1})
$X = V$	80.90	0.19
$X = NPR$	82.80	0.85

An example of a density scatter plot between observed frost depth FD and relative frost factor $FF_{rel,X,orb}(FD)$ for $X = V$ and $orb = (\text{ascending} + \text{descending})$ is shown in Fig. 4. The solid line shows the exponential model (4) evaluated for the corresponding fitting parameters provided in Table 2. Threshold values of relative frost factors $FF_{rel,X,orb}$ used to differentiate between the 'thawed' soil state and the 'frozen' soil state are indicated with the dashed lines (compare Table 3). These thresholds are defined as different levels of relative frost factor $FF_{rel,X,orb}(FD)$ achieved for very large frost depths FD . According to the definition (4) of the model $FF_{rel,X,orb}(FD)$ these thresholds are related to the value of the fitting parameter $A_{X,orb}$ for each method $X = V$ or NPR defined by Eqs. (1) and (2), respectively. For 'thawed' soil (soil state 0), the threshold value applied to the relative frost factors is $FF_{rel,X,orb} < 0.5 \cdot A_{X,orb} = 40.45\%$, while soil state 2 ('frozen') is assigned when $FF_{rel,X,orb} > 0.8 \cdot A_{X,orb} = 64.72\%$. The transitional soil state 1 ('partially frozen' or freezing in progress) is assigned when the relative frost factor $FF_{rel,X,orb}$ is in the corresponding intermediate range corresponding to $40.45\% \leq FF_{rel,X,orb} \leq 64.72\%$ for the example shown in Fig. 4.

Frozen soil (soil state 2) refers to soil states where frost depth FD exceeds the emission depth χ at L-band and consequently SMOS brightness temperatures T_B^{θ} become saturated and approach the winter maximum. However, soil texture and liquid water content heavily affect emission depth $\chi = 1/\gamma$ via effective soil permittivity $\epsilon_{soil} = \epsilon'_{soil} + i \cdot \epsilon''_{soil}$ which determines the power absorption coefficient $\gamma = 4\pi/\lambda \cdot \text{Im} \cdot \sqrt{\epsilon_{soil}}$ of the soil. At L-band wavelengths $\lambda = 21\text{ cm}$ and for frozen soils with $\epsilon'_{soil} \approx 5.5$ and $0.1 \leq \epsilon''_{soil} \leq 0.5$ emission depth is expected to be in the range of $8\text{ cm} \leq \chi \leq 15\text{ cm}$ (Hallikainen, Ulaby, Dobson, El-Rayes, & Wu, 1985; Mätzler, Ellison, Thomas, Sihvola, & Schwank, 2006; Rautiainen et al., 2012). According to these physical restrictions inherent in passive L-band measurements, the SMOS based soil F/T-state estimate does not intend to estimate the average frost depth FD within each grid cell, but rather to categorize the soil state into the three discrete states described in Table 3 and indicated in Fig. 4.

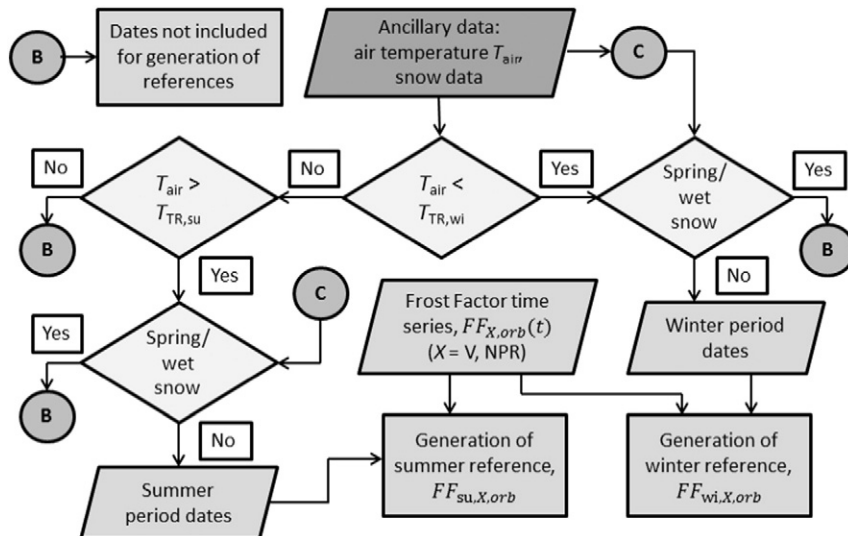


Fig. 3. Flow chart describing the logic of summer and winter reference generation.

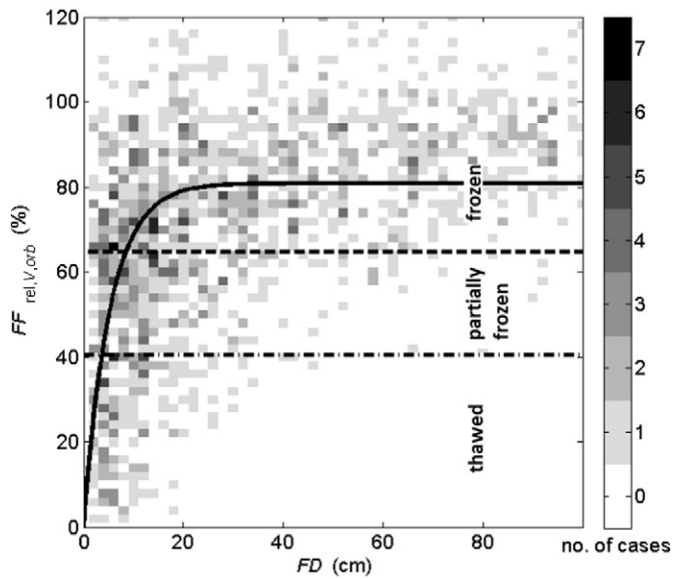


Fig. 4. Relative frost factors $FF_{rel,V,orb}$ (V-polarization method Eqs. (1) and (3), $orb =$ ascending + descending) versus *in situ* measured frost depth FD . Both ascending and descending orbits are shown, as well as the exponential fit (solid line, $A_{V,orb} = 80.9\%$ and $B_{V,orb} = 0.19 \text{ cm}^{-1}$) and the thresholds (dashed lines) used to distinguish between the three soil states 'frozen', 'partially frozen', 'thawed'.

Table 3
Soil state categories ($X = V, NPR$; $orb =$ ascending, descending).

Soil state:	Categorization condition in terms of	
Value	Description	$FF_{rel,X,orb}$ thresholds (%)
0	Thawed	$FF_{rel,X,orb} < 0.5 \cdot A_{X,orb}$
1	Partially frozen	$0.5 \cdot A_{X,orb} \leq FF_{rel,X,orb} \leq 0.8 \cdot A_{X,orb}$
2	Frozen	$FF_{rel,X,orb} > 0.8 \cdot A_{X,orb}$

3.5. Processing mask

To improve the quality of the soil F/T-state categorization achieved with our approach, a processing mask (PM) based on ancillary climatological data is applied. Information from ECMWF air temperatures T_{air} and the IMS snow mask data are combined (see Section 2.3) to gain information on the expected season for each EASE grid cell, hence enabling the distinction and exclusion of clearly erroneous soil F/T-state estimates.

The processing mask was chosen to have nine values as listed in Table 4. A moving average of 10 days was applied to the ECMWF air temperatures T_{air} to reduce the effect of daily variations. In order to determine $PM(t)$ for each EASE grid cell for the time (day) t , a constant set of criteria were used to define each value of PM . As several changes

Table 4
The nine values of processing mask $PM(t)$ for time t (day), criteria for their conditions, the respective seasons, and allowed transitions ($PM(t)$ to $PM(t+1)$). $T_{air}(t)$ denotes air temperature for time (day) t and $\langle T_{air} \rangle$ denotes average air temperature over 10 days.

$PM(t)$	Definition	Season	Definition criteria	Allowed transitions ($PM(t)$ to $PM(t+1)$)
0	Undetermined, or failure on determining the $PM(t)$	None		1, 3, 5, 7
1	Summer	Summer	$\langle T_{air} \rangle > 0 \text{ } ^\circ\text{C}$	0, 1, 2
2	First alarm of autumn	Summer	$T_{air}(t) \leq 0 \text{ } ^\circ\text{C}$	0, 1, 2, 3
3	Freezing period, early phase	Autumn	$\langle T_{air} \rangle \leq -1 \text{ } ^\circ\text{C}$	0, 1, 2, 3, 4
4	Freezing period, longer evolved	Autumn	$\langle T_{air} \rangle \leq -1 \text{ } ^\circ\text{C}$ and $T_{air}(t) < 0 \text{ } ^\circ\text{C}$ for 10 consecutive days	0, 4, 5
5	Winter	Winter	$\langle T_{air} \rangle \leq -3 \text{ } ^\circ\text{C}$	0, 5, 6
6	First alarm of spring	Winter	$T_{air}(t) > 0 \text{ } ^\circ\text{C}$	0, 5, 6, 7
7	Melting period	Spring	$\langle T_{air} \rangle > +3 \text{ } ^\circ\text{C}$ and snow is detected	0, 7, 8
8	End phase of melting period	Spring	$\langle T_{air} \rangle > +3 \text{ } ^\circ\text{C}$ and no snow is detected	0, 1

from a certain value to another were considered to be unlikely, such as a change from summer ($PM(t) = 1$) to the first alarm of spring ($PM(t) = 6$) without intermediate autumn and winter periods ($PM(t) = 2,3,4,5$), the value given for $PM(t)$ was restricted by $PM(t-1)$ for cases where the previous value was available. The criteria for selecting processing mask values for PM for the time unit t are given in Table 4, as well as allowed transitions between values from $PM(t)$ to $PM(t+1)$.

As an example, the hemispheric variability of two climatological events, calculated based on the processing mask for 2013, are illustrated in Fig. 5. The last date when the mask indicates summer ($PM(t) = 2$ in Table 4) are shown in panel a), and the first day when the mask indicates winter ($PM(t) = 5$ in Table 4) are depicted in panel b) in days after January 1st, 2013.

3.6. Final soil state estimates

Two soil F/T-state estimates are generated on a daily basis for the Northern Hemisphere EASE grid 1.0 data format: one categorizing the soil F/T-state using brightness temperatures at vertical polarization only ($FF_{rel,X,orb}$ with $X = V$ corresponding to definition (1)) and the one based on normalized polarization ratio ($FF_{rel,X,orb}$ with $X = NPR$ corresponding to definition (2)). Both estimates use observations from both $orb =$ ascending and $orb =$ descending orbits. Ascending orbit observations are applied over the Eurasian continent, while descending orbit overpasses are applied for Northern America. This decision is based on SMOS RFI probability information; descending orbits contain significant RFI contamination over Eurasia, while ascending orbits show more contamination over Northern America.

For the generation of the final soil F/T-state estimate, the processing mask detailed in Section 3.5 and Table 4, is applied over the soil F/T-states described in Table 3. The processing mask affects the final soil F/T-state estimate following the logic summarized in Table 5. For processing mask values $PM(t) = 3, 4, 7$ or 8 (freezing and melting periods), the mask has no effect on the F/T-state estimates. All soil F/T-state estimates are forced to the non-frozen category for $PM(t) = 1$ or 2 , which indicate a summer period. During the winter period ($PM(t) = 5$ or 6), no forcing from thawed soil state to the frozen soil category is applied: The only effect is that the soil state category value is not allowed to decrease; i.e. thawing is not allowed while air temperature T_{air} stays below the selected thresholds given in Table 4.

4. Demonstration of soil F/T-state retrieval

4.1. Soil F/T-state maps from SMOS for the northern hemisphere

Examples of SMOS soil F/T-state estimates over the northern hemisphere on November 1st, 2014 are depicted in Figs. 6–9, using different formulations (definitions (1) and (2)) of the relative frost factor $FF_{rel,X,orb}$ ($X = V, NPR$; $orb =$ ascending, descending). Corresponding maps of F/T-state categories 'frozen', 'thawed', and 'partially frozen' derived from $FF_{rel,NPR,orb}$ (Fig. 6 for $orb =$ ascending and Fig. 7 for

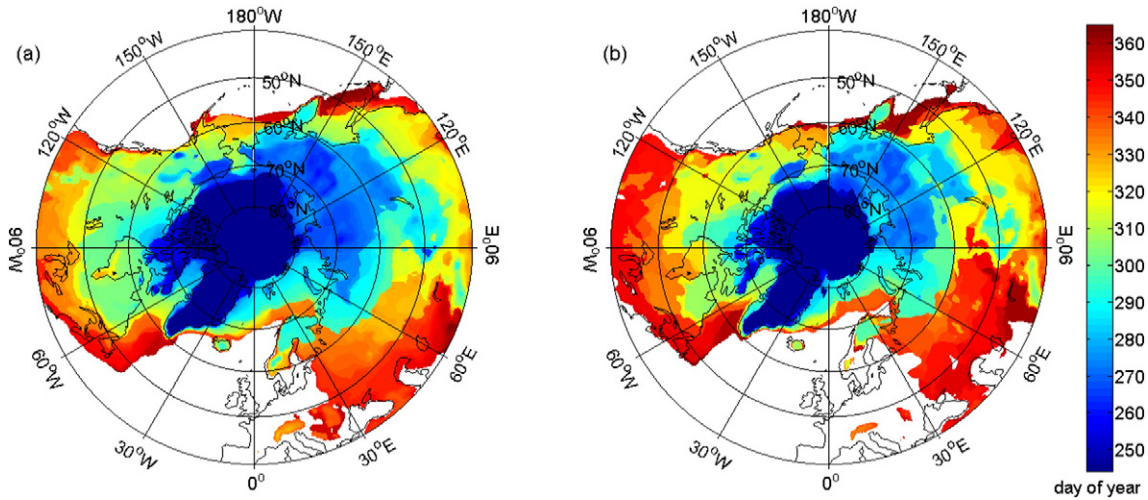


Fig. 5. Hemispheric variability of climatological events, calculated from the processing mask for 2013: (a) the last date (day of year) when the mask indicates summer ($PM(t) = 2$), and (b) the first day when the mask indicates winter ($PM(t) = 5$).

Table 5

The processing mask levels and their effect on to the final soil F/T-state estimates.

$PM(t)$	Effect on to the soil state estimate
1 or 2	Forces the soil state to category 0
3 or 4	No effect
5 or 6	No effect, if soil state category value increases but soil thawing (i.e. category value decrease) is not allowed
7 or 8	No effect

$orb =$ descending) and derived from $FF_{rel,V,orb}$ (Fig. 8 for $orb =$ ascending and Fig. 9 for $orb =$ descending) are shown. For each case, the effect of applying the processing mask described in Section 3.5 is illustrated by depicting both the unmasked estimate (panels a)) and the masked final soil F/T-state estimate (panels b)).

The extent of the areas categorized as ‘thawed’ corresponds with the geographical extent over which both versions ($X = V$ and NPR) of the algorithm could be applied. Beyond these areas, estimates of soil F/T-state could not be made either due to RFI, due to insufficient dynamic range between winter and summer references $FF_{wi,X,orb}$ and $FF_{su,X,orb}$, or due to lack of a proper winter reference ($FF_{wi,X,orb}$) as a result of

mild winter climate. For descending orbits (Figs. 7 and 9), notable portions of Asia are masked out, the main cause being contamination by RFI.

Similarly, it can be seen that ascending orbit estimates (Figs. 6 and 8) contain more grid cells masked out over North America, than descending orbit estimates. These were also masked out mainly due to RFI. Soil F/T-state estimates derived from $FF_{rel,V,orb}$ (Figs. 8 and 9) estimate smaller freeze areas, in particular over Eastern Europe, the Caucasus, as well as part of Alaska and Eastern Siberia, when compared to F/T-states derived from $FF_{rel,NPR,orb}$ (Figs. 6 and 7). The difference may be partially due to the effect of snow cover, which amplifies the signature (snow reduces the NPR similarly to soil freezing) typical for freezing for $FF_{rel,NPR,orb}$. However, another possible explanation is the low seasonal dynamics of brightness temperatures T_B^v at vertical polarization resulting in erroneous estimates.

4.2. Date of autumn soil freeze onset over the northern hemisphere

Autumn soil freezing onset dates were calculated from daily maps of SMOS F/T-states after applying the processing mask. The first instance of a given grid cell to be classified as ‘frozen’ (soil state 2 defined in Table 3) was determined to be the date of freezing onset ($DoF_x, X = V,$

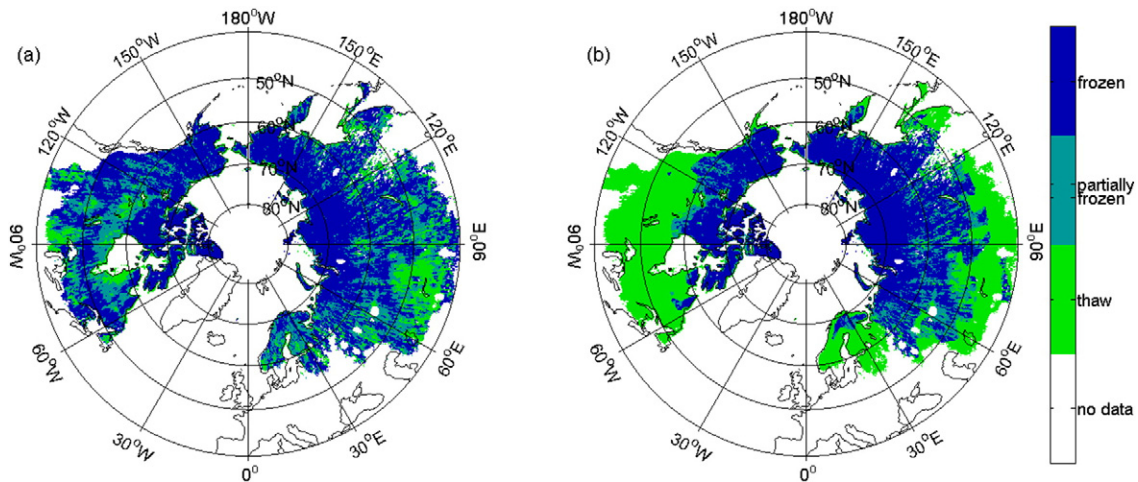


Fig. 6. Maps of SMOS soil F/T-state estimates over the northern hemisphere on November 1st 2014. F/T-state categories estimated from relative polarization index ($FF_{rel,X,orb}$ with $X = NPR$) for $orb =$ ascending orbits, before (a) and after (b) applying the processing mask. Extent of ‘thawed’ category depicts the geographical extent where the F/T-state categorization could be applied.

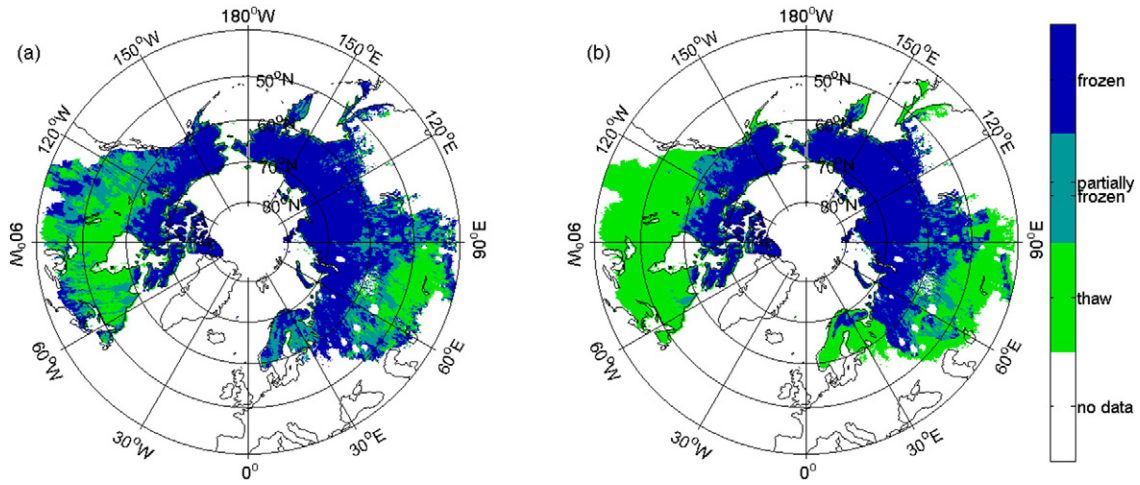


Fig. 7. Same as Fig. 6 ($X = \text{NPR}$) but for orb = descending orbits.

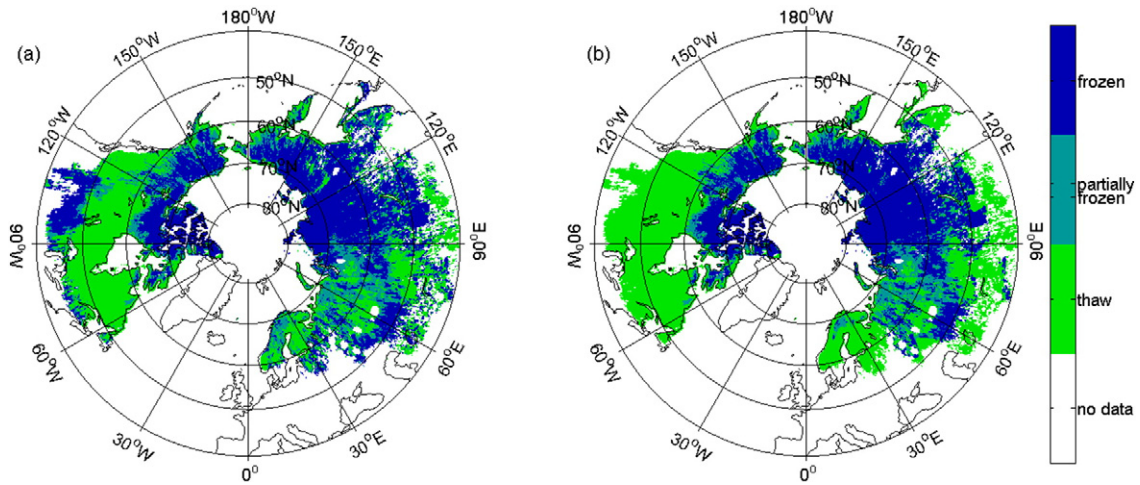


Fig. 8. Same as Fig. 6 but F/T-state categories are estimated from SMOS measurements at vertical polarization only ($FF_{\text{ret},X,\text{orb}}$ with $X = V$) for orb = ascending orbits.

NPR). The date was calculated from the F/T-state estimates derived for the two retrieval versions $X = \text{NPR}, V$ separately. Maps of the date of soil freezing (in day of year) for the autumn of 2013 are shown in Fig. 10 a–b, for the method $X = \text{NPR}$ and V , respectively.

In the figures, blue indicates an early date for freeze onset, while red indicates a later date. For 2013, the $X = V$ method can be seen to exclude large areas in particular over North America. Compared to the $X = \text{NPR}$ method, F/T-state estimates over Eurasia are likewise patchy with large

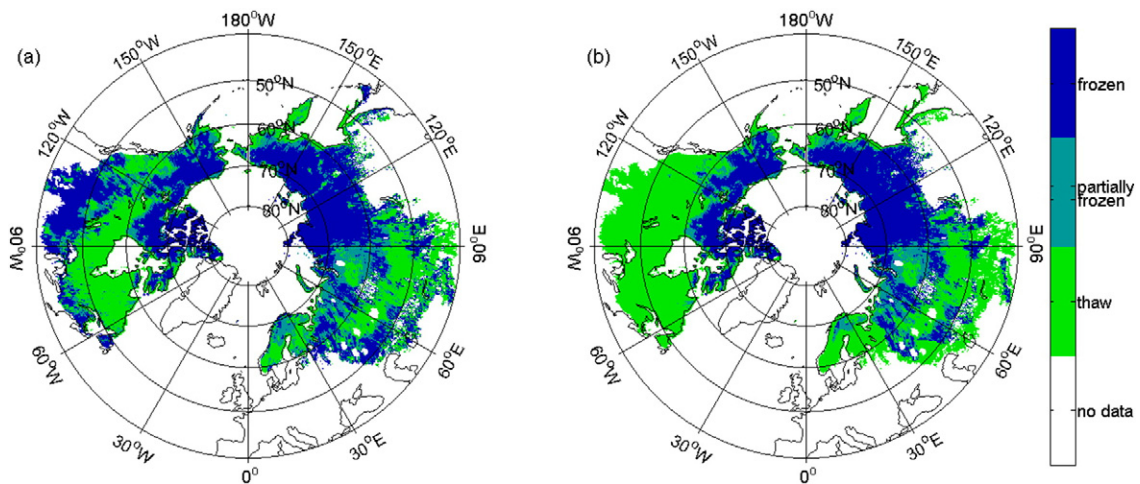


Fig. 9. Same as Fig. 8 ($X = V$) but for orb = descending orbits.

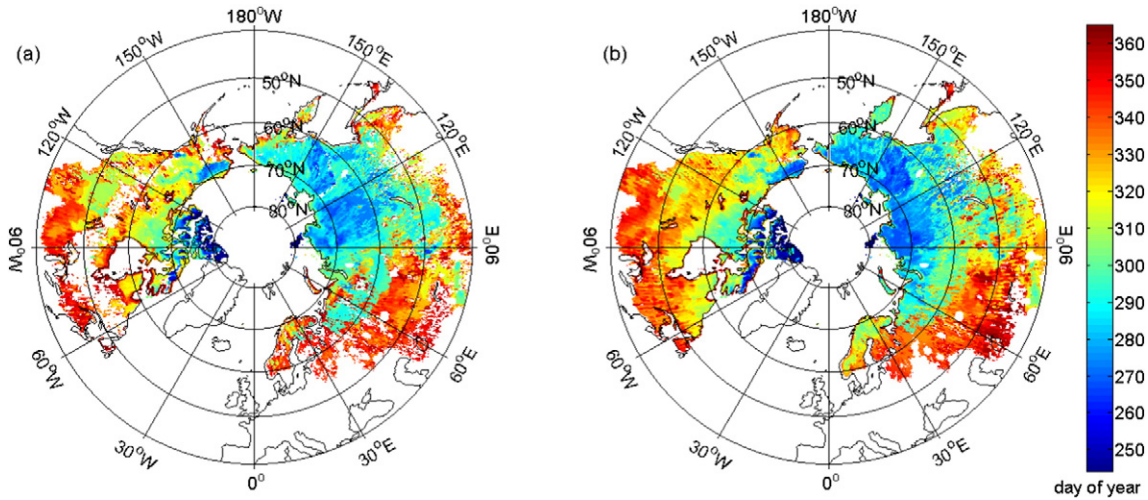


Fig. 10. Date of onset of soil freezing (DoF_x, X = V, NPR) for the year 2013 (day of year), defined from SMOS F/T-states estimated with version X = V (a) and X = NPR (b). Processing mask is applied.

missing areas over Eastern Europe and the Caucasus. This, again, is mainly due to low seasonal dynamics of brightness temperatures T_B^V at vertical polarization over those areas.

The freezing date identified for the autumn of 2013 is compared for the two methods (X = V, NPR) in Fig. 11, separately for Eurasia and North America, with statistics comparing the two methods given in Table 6. The differences between the two soil F/T-state retrieval methodologies (X = V, NPR) are smaller over North America, while larger differences are apparent over Eurasia. The bias between the methods was larger for North America, with freezing day estimates occurring on average five days later for the method X = V than for the method X = NPR. However, the rmse was smaller and correlation was better over North America. In some areas, both versions of the soil F/T-state algorithm (X = V or NPR) estimated soil freezing (F/T-state = ‘frozen’) to occur immediately after the summer flag was relaxed, forming the diagonals seen in Fig. 11. For these cases the freeze estimate was essentially based solely on the ancillary air temperature T_{air} masking procedure rather than from SMOS data.

The quality of SMOS soil F/T-state estimates was evaluated by comparing estimates with and without the processing mask. Instances where the processing mask was the sole driver of change in F/T-state were classified to be of low quality. For cases where SMOS soil F/T-

state gave a soil state estimate of ‘frozen’ more than three days after the processing mask, the estimate was considered to be of high quality. For all cases in between an intermediate level of quality was assigned. Examples of quality maps for the freeze onset day in 2013 are given in Fig. 12.

Comparisons of the soil freezing dates estimated from ECMWF soil level 2 temperatures and the two SMOS soil F/T-state estimates for 2013 are shown in Fig. 13. From ECMWF reanalysis data, soil was estimated to be frozen after level 2 soil temperatures consistently remained below 0 °C for a given grid cell. Both SMOS soil F/T-state methods using X = NPR (Fig. 13a) and X = V (Fig. 13b) show a consistent positive bias against freezing dates estimated from the ECMWF reanalysis data. Additional analysis of ECMWF reanalysis data against *in situ* observations, specifically over northern latitudes and during soil freezing periods, should be conducted in order to come to further conclusions on the reliability of SMOS based estimates. Albergel et al. (2015) have found ECMWF soil temperature data to be similar to that of corresponding *in situ* soil temperature observations on an annual basis and over regions with relatively moderate temperature variations (SNOTEL, SCAN and USCRN networks in USA and synoptic observations from Ireland, Germany, Czech Republic and Hungary in Europe).

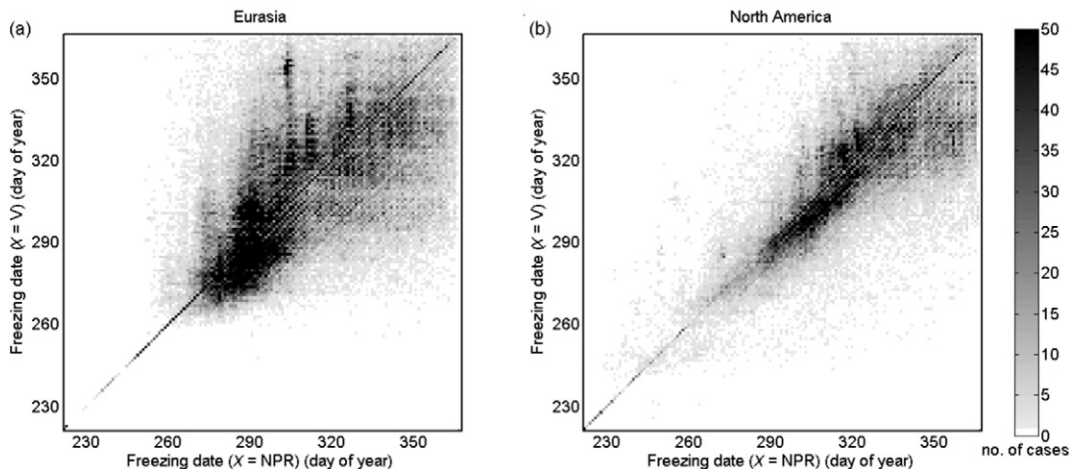


Fig. 11. Comparison of freezing dates in 2013 estimated with our soil F/T-state retrieval approach operated in the versions X = NPR (horizontal axis) and X = V (vertical axis). Comparison for Eurasia (a) and North America (b).

Table 6

Bias, rmse and coefficient of determination (r^2) of freezing dates in 2013 estimated with the soil F/T-state retrieval operated in the versions $X = \text{NPR}$, V for (a) Eurasia and (b) North America (statistics associated with Fig. 11).

	Bias (days)	rmse (days)	r^2 (days)
Eurasia	-0.28	19.8	0.44
North America	4.89	15.5	0.64

4.3. Time series over test sites

Time series of SMOS soil F/T-state estimates were analyzed over dedicated test sites, where *in situ* information on soil states were available (see Section 2.2.2). As an example, data for the Samoylov test site for the time period August 2010 to May 2013 are shown in Fig. 14. Time series of SMOS brightness temperatures T_B^p ($p = \text{H}, \text{V}$) from a single EASE grid pixel over the site is shown in panel a). Over the Samoylov site, winter and summer periods can be clearly identified from relatively low summer values (mean values for July: $T_B^{\text{H}} = 177.6 \text{ K}$ and $T_B^{\text{V}} = 229.0 \text{ K}$) compared to high winter values (mean value for February: $T_B^{\text{H}} = 210.8 \text{ K}$ and $T_B^{\text{V}} = 239.7 \text{ K}$). Panel b) shows soil F/T-state categories before applying the processing mask. At this site, even the unmasked F/T-states interpret most of the variations in T_B^p correctly as

'frozen' (soil state 2 defined in Table 3), when compared to *in situ* data on volumetric liquid soil water content (VWC_G , Fig. 14d) and ground temperature (T_G , Fig. 14e). The few clear misinterpretations along with method $X = \text{V}$ (red line in panel b)) during the summers of 2012, 2011 and 2014, as well as during the winter of 2012, were removed by the processing mask as can be seen in panel c) of Fig. 14. In the case of the Samoylov site, the processing mask removed the interpretation of 'partially frozen' soil (soil state 1 defined in Table 3) induced by the spring drop in T_B^p , induced by melting snow cover and eventual snow clearance.

An example of a more challenging site for the application of our soil F/T-state retrieval algorithm is the Gobbler's knob site in Alaska shown in Fig. 15. The area consists of dry tundra, with very muted annual dynamics in SMOS brightness temperatures of less than $\Delta T_B^{\text{H}} \approx 5.0 \text{ K}$ and $\Delta T_B^{\text{V}} \approx 1.3 \text{ K}$ at horizontal and vertical polarization, respectively. These muted dynamics are induced by dry soil, in particular the dryness of the surface soil (5 cm VWC_G in Fig. 15d) resulting in very similar effective permittivities and thus T_B^p for frozen and thawed soil states. As T_B^p during the winter tend to decrease due to very low physical ground temperatures T_G (panel e), in particular the soil F/T-states derived by the method $X = \text{V}$ suffer from misinterpretations of thawing soil in winter. Applying the processing mask removed most of these errors, but introduced some probable errors e.g. in the autumn of 2013. In the case of

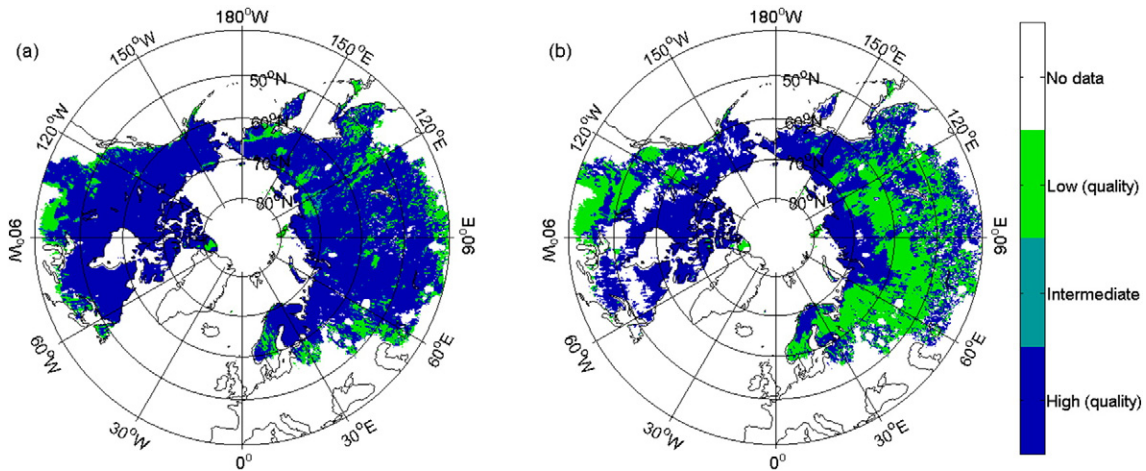


Fig. 12. Quality-level maps based on the degree of influence of the processing mask for method $X = \text{NPR}$ (a) and for method $X = \text{V}$ (b) for the freezing season of 2013. Cases where a change in the F/T-state is induced exclusively by the processing mask are categorized as low quality. For intermediate quality areas the soil is estimated to be frozen less than 3 days after the $PM(t)$ value has indicated the start of the freezing season.

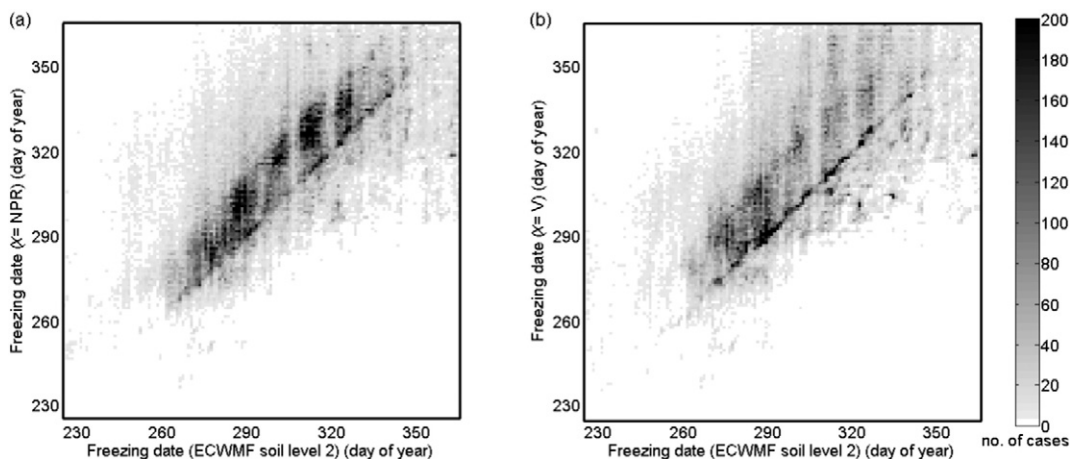


Fig. 13. Comparison between freezing date (day of year) estimated from ECMWF soil level 2 temperatures (horizontal axis) and SMOS soil F/T-state estimates (vertical axis) using the $X = \text{NPR}$ (a) and $X = \text{V}$ (b) methods.

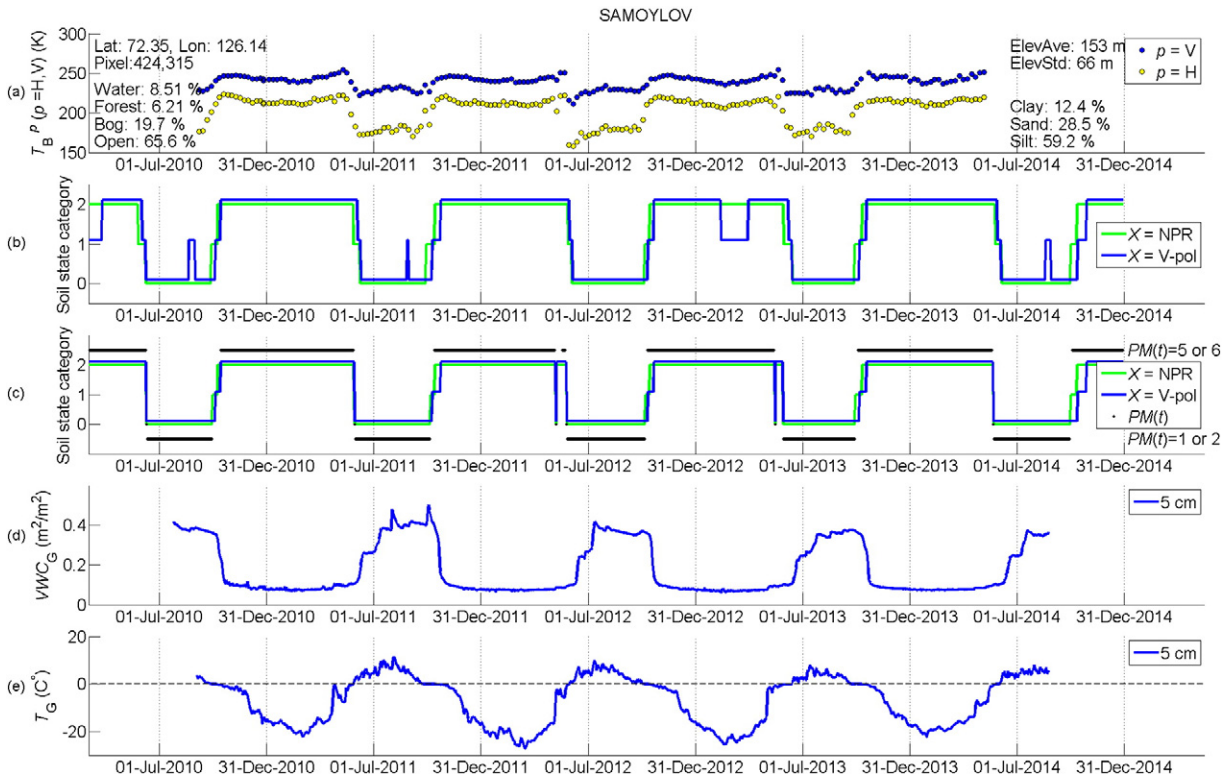


Fig. 14. Time series for Samoylov Island test site. a) weekly average of SMOS brightness temperatures T_B^P ($p = H, V$); b) soil state category for the method $X = V$ (red) and $X = NPR$ (blue) (2 = frozen, 1 = partially frozen, 0 = thawed); c) soil state category after applying processing mask, summer and winter seasons as given by processing mask are indicated with black lines; d) *in situ* volumetric soil moisture; and e) *in situ* soil temperature both at 5 cm depth.

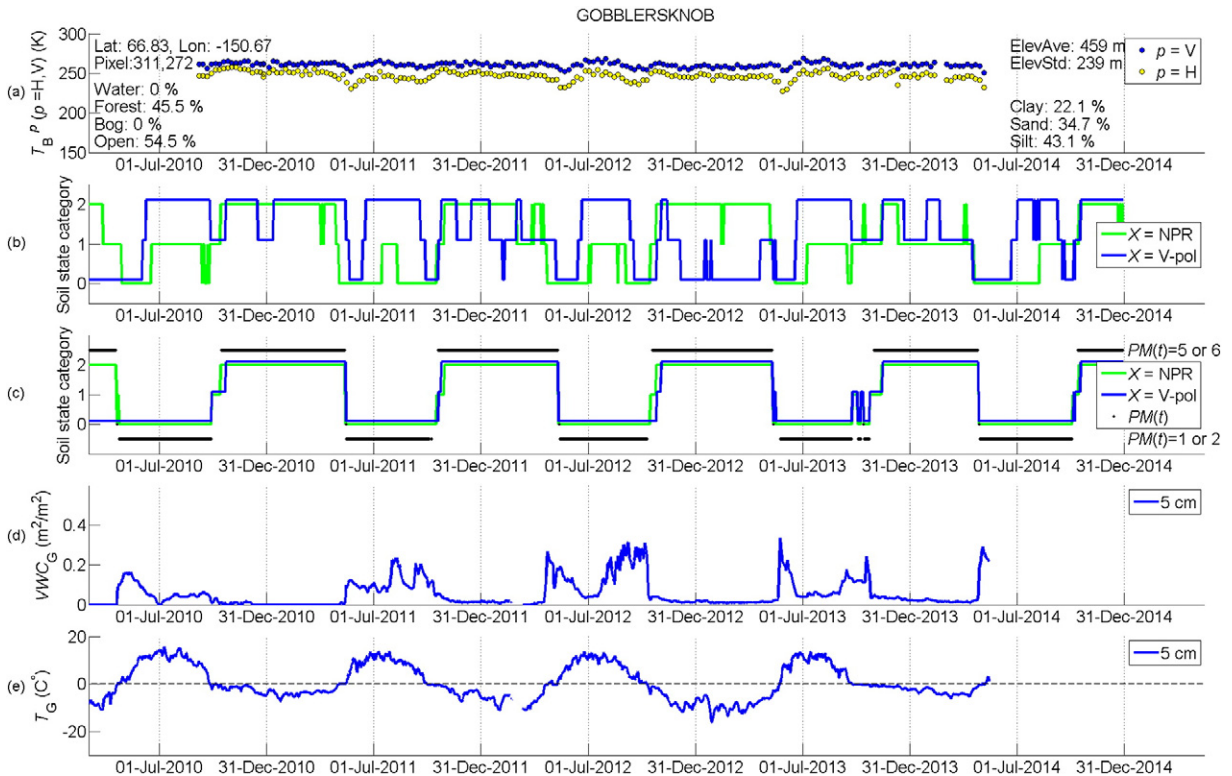


Fig. 15. Same as Fig. 14 but for Gobblers knob (SNOTEL) test site.

the Gobbler's knob test site, it is clear that the interpretation of the soil F/T-state could not be made without the application of the processing mask; the added value of the SMOS-based F/T-estimates themselves are therefore limited for this specific site.

A performance of our SMOS-based F/T-state product against information on soil F/T-state from several test sites is summarized in Fig. 16. The date of soil freezing estimated from SMOS (DoF_x , $X = V$, NPR) was compared to the soil freezing date assessed from both liquid soil moisture VWC_G and soil temperature T_G measured *in situ* at 5 cm depth ($DoF_{in situ}$, *in situ* = T_G , VWC_G). From these *in situ* data, the soil was considered to be frozen if a five day average of T_G was below 0 °C. The threshold value for *in situ* soil moisture observations was determined from the timing of abrupt VWC_G decreases and stabilization to a low value of *in situ* soil moisture, which represents the soil permittivity change due to soil freezing. For most of the sites soil was considered 'frozen' when a five day average of VWC_G was $<0.1 \text{ m}^3 \text{ m}^{-3}$. However, the threshold value varied from $0.05 \text{ m}^3 \text{ m}^{-3}$ to $0.2 \text{ m}^3 \text{ m}^{-3}$ depending on the typical soil-moisture conditions for a given area. The threshold value had to be manually optimized from the data for each site.

The very different spatial scales of the *in situ* data and the SMOS soil F/T-state estimates introduces many challenges for conducting comparisons. Most of the reference sites selected here contains observations taken only at single location (all SNOTEL sites and Rovaniemi). At Samylov Island test site, the measurements are taken from three locations, at Kolyma site from four locations and in Tiksi since 2013 from three locations. Only Sodankylä and Kenaston test areas include a larger observation network (as described in Section 2.2).

Using $X = V$ exhibited, on average, earlier freezing estimates than $X = NPR$ (bias of 6.8 and 1.3 days, compared to 16 and 7.8 days, when

compared to *in situ* = T_G and *in situ* = VWC_G respectively). It is also evident that the selected soil freezing thresholds for *in situ* observations were not consistent. This was expected, because it is very difficult to define the soil state based on observed soil temperature or moisture without any quantitative information on soil state for comparison, as the soil freezing temperature and corresponding permittivity is dependent on soil composition. Further research needs to be conducted for each reference site to define proper *in situ* determined soil freezing thresholds. The presented preliminary comparison results do not represent a complete validation of SMOS soil F/T-state estimates, nor provide comprehensive quantitative information on the quality of the product. Validation of satellite derived F/T estimates is challenging due to the rarity of corresponding *in situ* measurements and measurement networks representing the same scale and footprint.

For $X = V$, the unbiased root mean square error (urmse) was smaller and the correlation coefficient (r) was slightly better than for $X = NPR$. However, all sites excluding Kenaston are located in the Arctic region exhibiting large seasonal changes. For this climate region, using $X = V$ can be said to have an advantage over $X = NPR$ due to reduced sensitivity to snow cover.

Soil state estimates over the SNOTEL sites (triangles in Fig. 16) exhibited large deviations from *in situ* measurements. All SNOTEL sites reported only one location of observations representing the whole F/T product grid cell, which may be an underlying reason for the poor correlation for SNOTEL sites only ($r = 0.05$ and 0.37 for $X = NPR$ and *in situ* = T_G and VWC_G , respectively; $r = 0.36$ and 0.59 for $X = V$ and *in situ* = T_G and VWC_G , respectively). For the Cherskii and Tiksi sites DoF_x , $X = V$, NPR was systematically estimated later than observations from $DoF_{in situ}$, *in situ* = T_G , VWC_G were indicating.

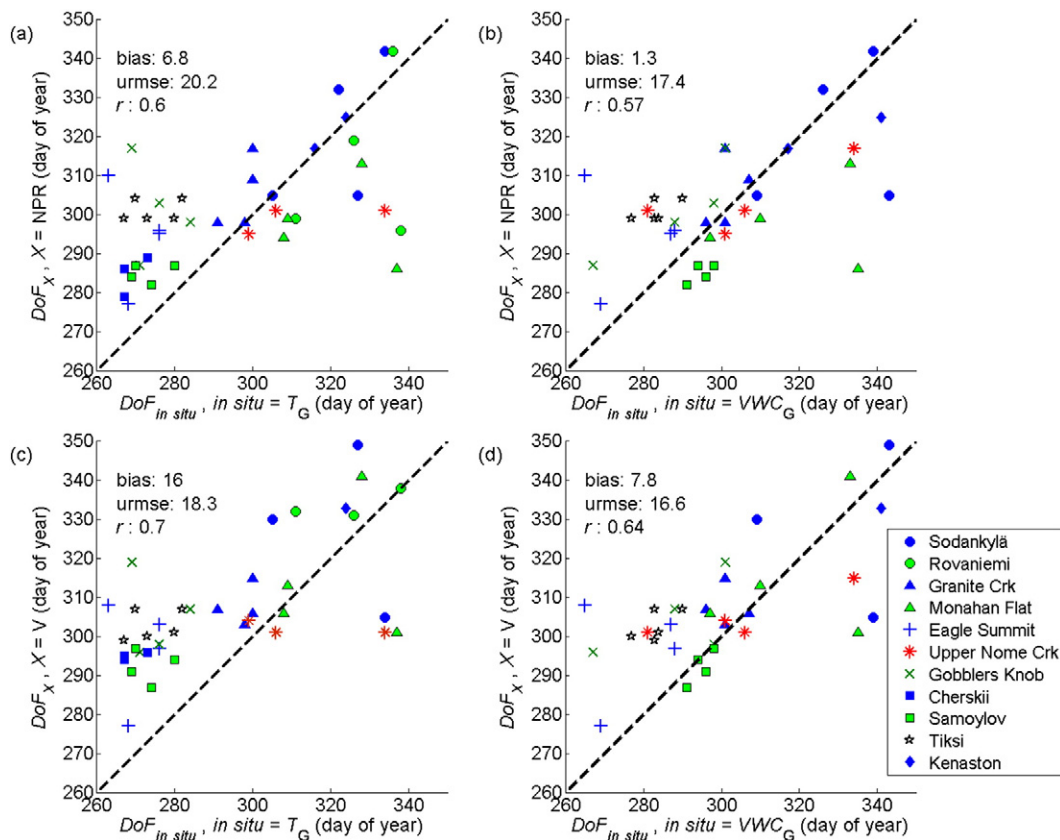


Fig. 16. Scatterplots with standard metrics of bias, unbiased rmse (urmse), and Pearson's correlation coefficient (r), for annual first freezing days estimated from the F/T-states based on SMOS data DoF_x with $X = V$ (panels c and d), $X = NPR$ (panels a and b) compared to freezing days estimated from *in situ* observations at 5 cm depth $DoF_{in situ}$, with *in situ* = T_G (soil temperatures, panels a and c), *in situ* = VWC_G (volumetric liquid water content, panels b and d).

5. Summary

Detection of soil freeze/thaw (F/T) state at the hemispheric-scale using SMOS Level-3 brightness temperatures $T_B^V(\theta)$ observed for incidence angles $50^\circ \leq \theta \leq 55^\circ$ was presented. The change detection approach draws on experience from earlier studies using tower-based L-band observations (Rautiainen et al., 2012, 2014) and theory-oriented studies (Schwank et al., 2014, 2015). Our soil F/T-state retrieval is evaluated for two different definitions of F/T-state proxies (frost factors $FF_{X,orb}$ defined by Eqs. (1) and (2)) represented either by brightness temperatures measured exclusively at vertical polarization (method $X = V$) or represented by normalized polarization ratios (method $X = NPR$). In both cases ($X = V$, NPR) the frost factors $FF_{X,orb}$ were used to compute corresponding relative (rel) frost factors $FF_{rel,X,orb}$ for each EASE grid cell based on summer- and winter references ($FF_{su,X,orb}$ and $FF_{wi,X,orb}$) representing thawed and frozen soil states, respectively. These summer- and winter references were derived for each grid cell individually based on the historical dataset of SMOS observations. The thresholds applied to the relative frost factors $FF_{rel,X,orb}$ to assign the three soil F/T-state categories ‘frozen’, ‘partially frozen’, and ‘thawed’ are based on comparison of SMOS observations to extensive soil frost depth measurements performed over Finland. Our study demonstrates the limitations of the empirical approach; empirically determined reference values $FF_{su,X,orb}$, $FF_{wi,X,orb}$ and fitting parameters $A_{X,orb}$, $B_{X,orb}$ are prone to uncertainties due to heterogeneous land cover and varying meteorological conditions over problematic areas. Future work is needed to supplement this study with physical models that are able to take into account e.g. changing snow conditions, and different land classes and soil types.

The motivation to explore the method $X = V$ was largely based on theoretical studies (Schwank et al., 2014, 2015), suggesting that $T_B^V(\theta \approx 50^\circ)$ were the least prone to effects of dry snow cover, while T_B^H at horizontal polarization were expected to be affected by the presence of dry snow in a manner similar to soil freezing. However, the signal of summer versus winter SMOS measurements $T_B^V(\theta \approx 50^\circ)$ theoretically favored to estimate soil F/T-states was insufficient in large parts of the northern hemisphere to allow proper function of our soil F/T-state detection algorithm. Moreover, winter estimates of soil state using the method $X = V$ experienced notable erroneous interpretations of thawing due to decreasing physical soil temperatures. In contrast, the method $X = NPR$ relying on normalized polarization ratios was less prone to retrieval errors caused by very low winter temperatures. However, the aforementioned effect of snow cover (Schwank et al., 2014, 2015) may induce the retrieval method $X = NPR$ to indicate soil freezing prematurely, with the presence of even a thin snow cover. False early freeze detection due to the effects of snow is problematic because snow is an effective thermal insulator, and acts to delay the onset of soil freezing as indicated by Rautiainen et al. (2014). Both methods $X = V$ and $X = NPR$ give similar results for soil freezing date for areas where freezing starts earlier (typically higher latitudes), while there are more differences in the estimates for areas with later soil freezing; illustrated in Fig. 11 as a wider spread in scatter plot towards later date of freezing. The fitting parameter $B_{X,orb}$, describing the curvature of the exponential fit, would indicate that $X = V$ method has better sensitivity to soil frost depth than $X = NPR$ method (Table 2). One possible explanation for this may be the different effect of the snow. Further efforts are needed to analyze the difference in more detail and to select optimal method for different areas.

The presented methodology to estimate soil F/T-states from SMOS data relies on a processing mask based on ancillary information on air temperature to eliminate clear misinterpretations of soil freezing during summer periods, and thawing during winter. Summer false freeze retrieval errors are most prominent over areas with dry mineral soils, because T_B^V observations resemble those induced by freezing events. The erroneous interpretations of winter thawing, on the other hand, are largely a result of reductions in physical temperatures, which also

decrease observed T_B^V . These errors could possibly be avoided by introducing physical temperature directly in the algorithm to estimate emissivity (in place of brightness temperature). However, in practice, attaining accurate soil surface temperature measurements globally is challenging and prone to other error sources. The applied processing mask may, however, introduce omission errors for cases where air temperature is not representative of actual local conditions.

The presented methodology applies to the autumn period of soil freezing. It is assumed that for snow covered areas, wet snow cover in spring effectively restricts the acquisition of information on soil F/T-state at L-band, due to the pronounced attenuation of microwaves in wet snow. However, initiatives are being undertaken to identify the period of spring melt and the occurrence of wet snow in general from SMOS observations (e.g. Pellarin et al., under review). Several studies have also been conducted for detection of snow melt at global scale using higher measurement frequencies (e.g. Hall, Kelly, Riggs, Chang, & Foster, 2002; Takala, Pulliainen, Huttunen, & Hallikainen, 2008; Takala, Pulliainen, Metsämäki, & Koskinen, 2009). This additional snow melt information can be used together with the autumn soil freezing information to derive comprehensive information on the freezing and thawing status of the soil for hydrological, climatological, and ecological applications.

Acknowledgments

This research was supported by European Space Agency projects “SMOS + Innovation: Application of SMOS data for the characterization of the freeze/thaw cycle and the retrieval of permafrost information” (ESA contract 4000105184/12/I-BG), “SMOS + Frost2 Study” (ESA contract 4000110973/14/NL/FF/lf), and the Finnish Academy Centre of Excellence in Atmospheric Science (272041). The authors would also like to thank the data providers: The Finnish Environment Institute (SYKE) for providing frost tube observation network data, International Soil Moisture Network (ISMN) and Natural Resources Conservation Service (NRCS) for providing SNOTEL data. SMOS data were obtained from the “Centre Aval de Traitement des Données SMOS” (CATDS), operated for the “Centre National d’Etudes Spatiales” (CNES, France) by IFREMER (Brest, France).

References

- Albergel, C., Dutra, E., Muñoz-Sabater, J., Haiden, T., Balsamo, G., Beljaars, A., et al. (2015). Soil temperature at ECMWF: an assessment using ground-based observations. *Journal of Geophysical Research – Atmospheres*, 120, 1361–1373. <http://dx.doi.org/10.1002/2014JD022505>.
- Arino, O., Ramos, P., Jose, J., Kalogerou, V., Bontemps, S., Defourny, P., et al. (2012). *Global Land Cover Map for 2009 (GlobCover 2009)*. European Space Agency (ESA) & Université catholique de Louvain (UCL). <http://dx.doi.org/10.1594/PANGAEA.787668>.
- Boike, J., Kattenstroth, B., Abramova, K., Bornemann, N., Chetverova, A., Fedorova, I., et al. (2013). Baseline characteristics of climate, permafrost and land cover from a new permafrost observatory in the Lena River Delta, Siberia (1998–2011). *Biogeosciences*, 10, 2105–2128. <http://dx.doi.org/10.5194/bg-10-2105-2013>.
- Dee, D. P., Uppala, S. M., Simmons, A. J., Berrisford, P., Poli, P., Kobayashi, S., et al. (2011). The ERA-interim reanalysis: configuration and performance of the data assimilation system. *Quarterly Journal of the Royal Meteorological Society*, 137(656), 553–597. <http://dx.doi.org/10.1002/qj.828>.
- Dorigo, W. A., Wagner, W., Hohensinn, R., Hahn, S., Paulik, C., Xaver, A., et al. (2011). The International Soil Moisture Network: a data hosting facility for global *in situ* soil moisture measurements. *Hydrology and Earth System Sciences*, 15, 1675–1698. <http://dx.doi.org/10.5194/hess-15-1675-2011>.
- Dorigo, W. A., Xaver, A., Vreugdenhil, M., Gruber, A., Hegyiová, A., Sanchis-Dufau, A. D., et al. (2013). GlobalAutomated quality control of *in situ* soil moisture data from the International Soil Moisture Network. *Vadose Zone Journal*, 12, 3. <http://dx.doi.org/10.2136/vzj2012.0097>.
- Entekhabi, D., Njoku, E. G., O'Neill, P. E., Kellogg, K. H., Crow, W. T., Edelstein, W. N., et al. (2010). The Soil Moisture Active Passive (SMAP) mission. *Proceedings of the IEEE*, 98(5), 704–716. <http://dx.doi.org/10.1109/JPROC.2010.2043918>.
- Fernandez-Moran, R., Wigneron, J. -P., Lopez-Baeza, E., Salgado-Hernanz, P. M., Mialon, A., Miernecki, M., et al. (2014). Evaluating the impact of roughness in soil moisture and optical thickness retrievals over the VAS area. *Proceedings of the IEEE International Geoscience and Remote Sensing Symposium 2014 (IGARSS'14)* (pp. 1947–1950).
- Fyodorov-Davydov, D. G., & Davydov, S. P. (2006). Seasonal thawing of soils on the north of the Kolyma lowland. In V. N. Kudeyarov (Ed.), *Soil Processes and Spatio-temporal Organization of Soils* (pp. 455–471). Moscow: Nauka (568 pp. (in Russian)).

- Hall, D. K., Kelly, R., Riggs, G., Chang, A. T. C., & Foster, J. L. (2002). Assessment of the relative accuracy of hemispheric-scale snow cover maps. *Annals of Glaciology*, 34, 24–30.
- Hallikainen, M. T., Ulaby, F. T., Dobson, M. C., El-Rayes, M. A., & Wu, L. -K. (1985). Microwave dielectric behavior of wet soil – part I: empirical models and experimental observations. *IEEE Transactions on Geoscience and Remote Sensing*, 23, 25–33.
- Helfrich, S., McNamara, D., Ramsay, B., Baldwin, T., & Kasheta, T. (2007). Enhancements to, and forthcoming developments in the interactive multisensor snow and Ice Mapping System (IMS). *Hydrological Processes*, 21, 1576–1586.
- Hollinger, D. Y., Goltz, S. M., Davidson, E. A., Lee, J. T., Tu, K., & Valentine, H. T. (1999). Seasonal patterns and environmental control of carbon dioxide and water vapour exchange in an ecotonal boreal forest. *Global Change Biology*, 5, 891–902.
- Iwata, Y., Hirota, T., Suzuki, T., & Kuwao, K. (2012). Comparison of soil frost and thaw depths measured using frost tubes and other methods. *Cold Regions Science and Technology*, 71, 111–117.
- Kaleschke, L., Tian-Kunze, X., Maaß, N., Mäkynen, M., & Drusch, M. (2012). Sea ice thickness retrieval from SMOS brightness temperatures during the Arctic freeze-up period. *Geophysical Research Letters*, 39(5), 5501. <http://dx.doi.org/10.1029/2012GL050916>.
- Kerr, Y., Waldteufel, P., Wigneron, J. -P., Martinuzzi, J. -M., Font, J., & Berger, M. (2001). Soil moisture retrieval from space: the soil moisture and ocean salinity (SMOS) mission. *IEEE Transactions on Geoscience and Remote Sensing*, 39(8), 1729–1735.
- Kerr, Y. H., Waldteufel, P., Wigneron, J. -P., Delwart, S., Cabot, F., Boutin, et al. (2010). The SMOS mission: new tool for monitoring key elements of the global water cycle. *Proceedings of the IEEE*, 98(5), 666–687.
- Khazaal, A., & Anterrieu, E. (2009). SMOS image reconstruction algorithm: extension of the band limited approach to the fully-polarimetric mode of MIRAS. *ACTEA '09. International Conference on Advances in Computational Tools for Engineering Applications* (pp. 180–185). <http://dx.doi.org/10.1109/ACTEA.2009.5227912>.
- Kim, Y., Kimball, J., McDonald, K., & Glassy, J. (2011). Developing a global data record of daily landscape freeze/thaw status using satellite passive microwave remote sensing. *IEEE Transactions on Geoscience and Remote Sensing*, 49(3), 949–960.
- Kim, Y., Kimball, J., Zhang, K., & McDonald, K. (2012). Satellite detection of increasing northern hemisphere non-frozen seasons from 1979 to 2008: implications for regional vegetation growth. *Remote Sensing of Environment*, 121, 472–487.
- Langer, M., Westermann, S., Muster, S., Piel, K., & Boike, J. (2011). The surface energy balance of a polygonal tundra site in northern Siberia part 2: winter. *The Cryosphere*, 5, 509–524.
- Lawrence, H., Wigneron, J. -P., Richaume, P., Novello, N., Grant, J., Mialon, A., et al. (2014). Comparison between SMOS vegetation optical depth products and MODIS vegetation indices over crop zones of the USA. *Remote Sensing of Environment*, 140, 396–406.
- Leavesley, G., David, O., Garen, D., Goodbody, A., Lea, J., Marron, J., et al. (2010). A modeling framework for improved agricultural water-supply forecasting. *2nd Joint Federal Interagency Conference, Las Vegas, Nevada, June 27–July 1, 2010*.
- Lemmetyinen, J., Schwank, M., Rautiainen, K., Kontu, A., Parkkinen, T., Mätzler, C., et al. (2015). Snow density and ground permittivity retrieved from L-band radiometry: application to experimental data. *Remote Sensing of Environment* (under review).
- Liebner, S., Ganzert, L., Kiss, A., Yang, S., Wagner, D., & Svenning, M. M. (2015). Shifts in methanogenic community composition and methane fluxes along the degradation of discontinuous permafrost. *Frontiers in Microbiology*, 6.
- Mäkinen, R., & Orvomaa, M. (2012). Roudan seuranta Suomessa luonnontilaisilla mailla. In T. Maasilta (Ed.), *Vesitalous* (pp. 6–11) (Forssa, Finland (in Finnish)).
- Martin-Neira, M., & Goutule, J. M. (1997). A two-dimensional aperture synthesis radiometer for soil moisture and ocean salinity observations. *ESA Bulletin*, 92, 95–104.
- Mätzler, C., Ellison, W., Thomas, B., Sihvola, A., & Schwank, M. (2006). Dielectric properties of natural media. In C. Mätzler (Ed.), *Thermal Microwave Radiation: Applications for Remote* (pp. 427–539). <http://dx.doi.org/10.1049/PBEW052E>.
- Mecklenburg, S., Drusch, M., Kerr, Y. H., Font, J., Martin-Neira, M., Delwart, S., et al. (2012). ESA's soil moisture and ocean salinity mission: mission performance and operations. *IEEE Transactions on Geoscience and Remote Sensing*, 50, 1354–1366.
- Mironov, V. L., Muzalevskiy, K. V., & Savin, I. V. (2013). Retrieving temperature gradient in frozen active layer of Arctic tundra soils from radiothermal observations in L-band—theoretical modeling. *IEEE Journal of Selected Topics in Applied Earth Observations and Remote Sensing*, 6, 1781–1785.
- Muster, S., Langer, M., Heim, B., Westermann, S., & Boike, J. (2012). Subpixel heterogeneity of ice-wedge polygonal tundra: a multi-scale analysis of land cover and evapotranspiration in the Lena River delta, Siberia. *Tellus B*, 64, 17301. <http://dx.doi.org/10.3402/tellusb.v64i0.17301>.
- Naeimi, V., Paulik, C., Bartsch, A., Wagner, W., Kidd, R., Sang-Eun, P., ... Boike, J. (2012). ASCAT surface state flag (SSF): extracting information on surface freeze/thaw conditions from backscatter data using an empirical threshold-analysis algorithm. *IEEE Transactions on Geoscience and Remote Sensing*, 50(7), 2566–2582.
- Oliva, R., Daganzo-Eusebio, E., Kerr, Y., Mecklenburg, S., Nieto, S., Richaume, P., et al. (2012). SMOS radio frequency interference scenario: status and actions taken to improve the RFI environment in the 1400–1427-MHz passive band. *IEEE Transactions on Geoscience and Remote Sensing*, 50(5), 1427–1439.
- Pellarin, T., Mialon, A., Biron, R., Coulaud, C., Gibon, F., Kerr, Y., et al. (2015). Three-year of L-band brightness temperature measurements in mountainous area: topography, vegetation and snow melting issues (This RSE special issue, under review).
- Rautiainen, K., Lemmetyinen, J., Pulliainen, J., Vehviläinen, J., Drusch, M., Kontu, A., et al. (2012). L-band radiometer observations of soil processes at boreal and sub-Arctic environments. *IEEE Transactions on Geoscience and Remote Sensing*, 50(5), 1483–1497.
- Rautiainen, K., Lemmetyinen, J., Schwank, M., Kontu, A., Menard, C. B., Mätzler, C., et al. (2014). Detection of soil freezing from L-band passive microwave observations. *Remote Sensing of Environment*, 147, 206–218. <http://dx.doi.org/10.1016/j.rse.2014.03.007>.
- Rignot, E., & Way, J. (1994). Monitoring freeze/thaw cycles along north-south Alaskan transects using ERS-1 SAR. *Remote Sensing of Environment*, 49, 131–137.
- Roy, A., Royer, A., Derksen, C., Brucker, L., Langlois, A., Mialon, A., & Kerr, Y. H. (2015). Evaluation of spaceborne L-band radiometer measurements for terrestrial freeze/thaw retrievals in Canada. *IEEE Journal of Selected Topics in Applied Earth Observations and Remote Sensing*. <http://dx.doi.org/10.1109/JSTARS.2015.2476358>.
- Schwank, M., Mätzler, C., Wiesmann, A., Wegmüller, U., Pulliainen, J., Lemmetyinen, J., K., et al. (2015). Snow density and ground permittivity retrieved from L-band radiometry: a synthetic analysis. *IEEE Journal of Selected Topics in Applied Earth Observations and Remote Sensing*, 8(8), 1–14. <http://dx.doi.org/10.1109/JSTARS.2015.2422998>.
- Schwank, M., Rautiainen, K., Mätzler, C., Stähli, M., Lemmetyinen, J., Pulliainen, J., et al. (2014). Model for microwave emission of a snow-covered ground with focus on L band. *Remote Sensing of Environment*, 154(8), 180–191. <http://dx.doi.org/10.1016/j.rse.2014.08.029>.
- Schwank, M., Stähli, M., Wydler, H., Leuenberger, J., Mätzler, C., & Flüher, H. (2004). Microwave L-band emission of freezing soil. *IEEE Transactions on Geoscience and Remote Sensing*, 42(6), 1252–1261.
- Schwank, M., Wiesmann, A., Werner, C., Mätzler, C., Weber, D., Murk, A., et al. (2010). ELBARA II, an L-band radiometer system for soil moisture research. *Sensors*, 10, 584–612. <http://dx.doi.org/10.3390/s100100584>.
- Skogland, T., Lomeland, S., & Goksoyr, J. (1988). Respiratory burst after freezing and thawing of soil: experiments with soil bacteria. *Soil Biology and Biochemistry*, 20, 851–856.
- Smith, S., & Brown, J. (2009). Permafrost. Permafrost and seasonally frozen ground. Assessment of the status of the development of standards for the terrestrial essential climate variables. *Global Terrestrial Observing System* (22 pp., version 13, 8 May 2009, Rome, 2009).
- Takala, M., Pulliainen, J., Huttunen, M., & Hallikainen, M. (2008). Detecting the onset of snow melt using SSM/I data and the self-organizing map. *International Journal of Remote Sensing*, 29(3/4), 755–766.
- Takala, M., Pulliainen, J., Metsämäki, S., & Koskinen, J. (2009). Detection of snowmelt using spaceborne microwave radiometer data in Eurasia from 1979 to 2007. *IEEE Transactions on Geoscience and Remote Sensing*, 47(9), 2996–3000.
- Wang, J. R., & Schmugge, T. (1980). An empirical model for the complex dielectric permittivity of soils as a function of water content. *IEEE Transactions on Geoscience and Remote Sensing*, GE-18, 288–295.
- Wigneron, J. -P., Kerr, Y., Waldteufel, P., Saleh, K., Escorihuela, M. J., Richaume, P., et al. (2007). L-band microwave emission of the biosphere (L-MEB) model: description and calibration against experimental datasets over crop fields. *Remote Sensing of Environment*, 107, 639–655.
- Zhang, L., Zhao, T., Jiang, L., & Zhao, S. (2010). Estimate of phase transition water content in freeze-thaw process using microwave radiometer. *IEEE Transactions on Geoscience and Remote Sensing*, 48(12), 4248–4255.
- Zhang, T., Barry, R. G., Knowles, K., Ling, F., & Armstrong, R. L. (2003). Distribution of seasonally and perennially frozen ground in the Northern Hemisphere. In M. Phillips, S. M. Springman, & L. U. Arenson (Eds.), *Proceedings of the 8th international conference on permafrost*, 21–25. Zurich, Switzerland (pp. 1289–1294). Lisse, The Netherlands: A.A. Balkema.
- Zhao, T., Zhang, L., Jiang, L., Zhao, S., Chai, L., & Jin, R. (2011). A new soil freeze/thaw discriminant algorithm using AMSR-E passive microwave imagery. *Hydrological Processes*, 25(11), 1704–1716.
- Zreda, M., Zeng, X., Shuttleworth, J., Zweck, C., Ferre, T., Franz, T., et al. (2011). Cosmic-ray neutrons, an innovative method for measuring area-average soil moisture. *GEWEX News*, 21(3), 6–10.
- Zuerndorfer, B., & England, A. W. (1992). Radiobrightness decision criteria for freeze/thaw boundaries. *IEEE Transactions on Geoscience and Remote Sensing*, 30(1), 89–102.